Single Crystal Growth and Characterization of Silicon Germanium Alloys

by

Tilghman L. Rittenhouse

B.S. Materials Science and Engineering
United States Air Force Academy, 1994

Submitted to the Department of Materials Science and Engineering
in Partial Fulfillment of the Requirements for the Degree of
Master of Science in Materials Science and Engineering

at the

Massachusetts Institute of Technology

February 1999

Signature of Author: ______________________________
Department of Materials Science and Engineering
January 15, 1999

Certified by: ______________________________
August F. Witt
Ford Professor of Engineering, Margaret MacVicar Faculty Fellow
Thesis Supervisor

Accepted by: ______________________________
Linn W. Hobbs
John F. Elliott Professor of Materials
Chairman, Departmental Committee on Graduate Students

Single Crystal Growth and Characterization of Silicon Germanium Alloys

by

Tilghman L. Rittenhouse

Submitted to the Department of Materials Science and Engineering
on January 15, 1999 in Partial Fulfillment of the
Requirements for the Degree of Master of Science in
Materials Science and Engineering

ABSTRACT

Silicon and germanium exhibit complete solid solubility for all binary concentrations. However, the growth of single crystalline SiGe alloys by bulk growth processes is hindered by the relatively wide separation of the solidus and liquidus lines. Previous research has yielded single crystals grown by the Czochralski method which are limited to only a few atomic percent of solute (Si or Ge), and even these crystals must be grown slowly (on the order of a millimeter per hour). On both a macroscopic and a microscopic scale, these crystals exhibit large axial variation in the solute distribution.

This research investigates Si_xGe_{1-x} alloys with $0<x\leq0.05$. Several growth parameters that affect axial and radial segregation as well as growth interface stability and microsegregation are investigated. Specifically, this research investigates methods to influence the Si axial composition fluctuations, minimize dislocation density in the crystal, and allow for a relatively fast growth rate while maintaining single crystalline growth.

In the reported growth experiments, single crystalline growth was limited to boule concentrations of less than 1 at% Si. For this concentration range of Si, the growth rate could be varied; this work resulted in single crystalline growth for growth rates between 2 and 11 mm/hr. For the thermal configuration used, concentrations of Si higher than 1 at% resulted in all instances in polycrystalline growth regardless of the growth rate.

Axial macrosegregation of solute in the boule was found to lie in the middle of values reported in the literature. The effective distribution coefficient (k_{eff}) of Si in the concentration range investigated was found to be 2.75. Seed rotation rate variations between 15 and 45 rpm were not found to affect the macrosegregation of solute, indicating segregation was dominated by convective currents and not a solute boundary layer (diffusion).

The dislocation density was high ($\sim10^5/cm^2$) in regions of the boules in which the Si concentration was relatively high (~1 at% Si). In other portions of the boules in which the

Si concentration was below minimum detection limits (0.0177 at% Si), the boules were observed to grow dislocation-free.

Thesis Supervisor: August F. Witt
Title: Ford Professor of Engineering, Margaret MacVicar Faculty Fellow

TABLE OF CONTENTS

LIST OF ILLUSTRATIONS AND FIGURES

LIST OF TABLES

ACKNOWLEDGMENTS

First and foremost, I owe many thanks to the Massachusetts Institute of Technology and specifically the Department of Materials Science and Engineering. The department's support of me academically, emotionally, and in terms of funding was critical in the completion of this work. Many people within the department are owed my personal thanks. Professor August Witt was an endless supply of information, aided me in identifying the phenomena I encountered in my work, and provided valuable guidance in devising experimental and analytical protocol. Likewise, Dr. Piotr Becla aided me in learning many different characterization techniques, was an expert on all of the hardware I had to learn from the point of zero knowledge, and instructed me when I grew my first crystal. Mr. John DiFrancesco also tolerated my daily visits of questions and requests for help in physically setting up the hardware I used. Both Ms. Ann Jacoby and Ms. Gloria Landahl constantly helped me on the academic side of the house, and I owe particular thanks to Ann for having the patience to work with my ever-changing schedule. Also, Mr. Joe Adario taught me many of the X-ray analysis tools used in this research, and I owe thanks to Dr. Neel Chatterjee in the Environment and Planetary Sciences center for his help in learning how to conduct the electron beam microprobe analysis. In addition my fellow students, Frank Johnson and Yu Zheng, provided thoughtful insight.

I owe additional thanks for other sources of funding for this research. I thank the Air Force for providing me the opportunity to return to the academic environment, and I only hope I can become an asset to the defense community because of the time they allowed me to improve my research skills. I also thank NASA, who provided much of the funding for my research.

CHAPTER ONE: INTRODUCTION

Silicon germanium (SiGe) bulk alloys have numerous potential applications. These applications stem primarily from the fact that SiGe alloys have favorable electrical properties (such as a higher hole mobility) and an adjustable bandgap. Currently, SiGe is used as a thermoelectric power generator in portable terrestrial units as well as in satellite systems that penetrate deep space (1,2). SiGe can also be used as a photodetector (3). Because SiGe is amenable to bandgap engineering, SiGe can be utilized as a substrate material for III-V compound semiconductors. Therefore, SiGe can serve as the basis for optoelectronics - the integration of electronic and photonic devices. Finally, SiGe is a candidate for solar cells since the material can be tailored for maximum conversion of solar radiation (4,5).

The phase diagram of SiGe (fig 1) shows complete liquid and solid solubility. Therefore, it is theoretically possible to produce bulk alloys that have a range of lattice parameters between those of pure Si and pure Ge. However, previous attempts at bulk growth of SiGe reported in the literature have been unsuccessful in producing boules with properties suitable for device fabrication.

The Czochralski technique poses several complications for growth of device quality SiGe alloys. First, there is a high degree of macroscopic axial segregation when growing SiGe from a melt in batch operation. In addition, any thermal asymmetry in Czochralski growth will result in the formation of rotational striations (i.e., inhomogeneous distribution of the dopant in the radial direction). Further challenges are posed by density and surface tension induced convection in the melt. Convective currents lead to uneven dopant incorporation in the crystal (non-rotational striations) which can foster the generation of defects. Finally, the onset of constitutional supercooling and related growth interface instabilities and breakdown are difficult to control during growth by the Czochralski technique.

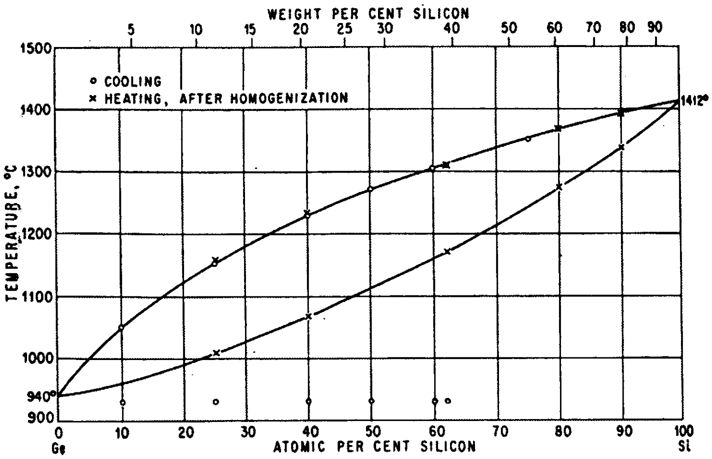

Figure 1. Phase diagram for the Si-Ge system. Reference 6

Because of the difficulties mentioned above in regard to Czochralski growth of SiGe, much of the SiGe produced today is grown via vapor deposition (7). In recent years, SiGe superlattices have generally been formed as buffer layers deposited on Si substrates by molecular beam epitaxy or chemical vapor deposition (8). However, if bulk SiGe single crystals can be produced instead of the current practice of using Si substrates, lattice mismatch stress can be reduced or eliminated (8). Therefore, there is a need for bulk single crystals over the entire Si_xGe_{1-x} composition range.

The Bridgman growth technique has better temperature stability in the melt than Czochralski growth (the liquid on top of the solid is more stable in terms of buoyancy effects) (8). However, although Bridgman growth provides for greater melt stability, it imposes limitations in crystal diameter and is subject to complications related to the requirement of a confining crucible (9). Therefore, for this study, Czochralski growth was selected due to its promise as a bulk growth technique that may be used in an industrial setting.

The present work is directed at identifying heat transfer effects during growth. First investigated will be parameters affecting the macroscopic composition and crystallinity of the bulk alloy. Parameters to be studied include the melt composition, the growth rate, and the rate of seed rotation. Also, the compositional and structural perfection of the grown crystals is examined on a microscale over macroscopic dimensions. Features of interest to this study include the presence of rotational and non-rotational striations, the formation of growth facets, and the density and distribution of dislocations.

CHAPTER TWO: OUTLINE OF OBJECTIVES AND APPROACH

2.1 Objectives of Research

This research intends to determine a cause-and-effect relationship between controllable growth parameters of bulk single crystals and crystal properties that are of significance to device applications. The controllable Czochralski growth input parameters manipulated in this investigation include the growth rate, the seed rotation rate, the axial and radial thermal gradients, the thermal symmetry of the system, and the starting composition of the melt. Resulting crystal properties of interest include the macroscopic and microscopic Si concentration in the axial and radial directions, facet formation in the boule, dislocation density, and structural perfection (including the ability to produce a single crystal).

Specific target values were set given the results reported in the literature. *(1)* First, a single crystal of 5 at% Si that measured 1 cm in diameter and 5 cm in length was one goal. *(2)* Also, the crystal was to have a dislocation density no greater than $10^5/\text{cm}^2$. *(3)* Finally, by analyzing several of the crystals grown, a repeatable value for the segregation coefficient was to be determined for the particular growth conditions used in this work.

2.2 Approach

2.2.1 Theory

The large separation of the solidus and liquidus lines in the SiGe phase diagram makes the constituent distribution extremely sensitive to small changes in the growth conditions, which can lead to excessive inhomogeneities and strain. Compositional inhomogeneities in electronic materials have a direct effect on their electronic properties (10) and adversely influence device characteristics (11,12) and performance. Strain in the growing crystal leads to the formation of dislocations and eventually to polygonization in the form of low-angle grain boundaries. As a result, critical solidification velocities for SiGe reported in the literature are on the order of only a few mm/hr (13).

Thermal asymmetry can produce problems in Czochralski growth. As the growing crystal is rotated, radial thermal asymmetry can cause portions of the boule to melt and resolidify at different rates depending on radial position. The thermal asymmetry can be caused by either radial temperature fluctuations in the melt or by a physical misalignment of the center of the boule over the center of the melt. Regardless of the cause of the thermal asymmetry, an unstable (asymmetric) interface in which the growth rate oscillates will result. Rotational striations then develop in the boule in which the solute concentration forms bands perpendicular to the growth axis.

Density and surface tension induced convection also cause problems in Czochralski growth. If the seed is subject to very slow or no rotation, surface tension driven or density driven convection controls the characteristics of the solute boundary layer at the crystal-melt interface. This leads to time-dependent microsegregation of the constituents (non-rotational striations) as well as the generation of defects. Forced convection induced by rotating the seed can aid in alleviating this problem of temperature fluctuations by making the convection time-independent.

Constitutional supercooling is yet another difficulty that must be considered when performing Czochralski growth. Constitutional supercooling occurs when the liquid ahead of the interface becomes rich in rejected constituent, increasing the supercooling in the immediate vicinity of the crystal. The freezing temperature of the melt near the solid-liquid interface can be greater than the actual temperature of the liquid (controlled by the applied temperature gradient). Growth rate and boundary layer fluctuations can result. Thus, constitutional supercooling can ultimately result in an unstable interface (with related segregation effects) as well as in actual growth interface breakdown (leading to cellular growth).

All of the conditions listed above result in variations in the growth of a crystal with time, and therefore an inhomogeneous boule is grown. Much of the current theory that models macrosegregation, microsegregation, defect generation, etc., relates to the steady-state condition. However, in reality, Czochralski growth of SiGe is never in a dynamic steady-state condition given the current technology. Therefore, this work attempts to investigate methods to eliminate or alleviate the deleterious growth conditions detailed above, as well as provide data to link steady-state theory to actual growth conditions and results.

As a basis for the present work, several SiGe crystal properties can be predicted by reviewing previously published results found in the literature. For example, published values for silicon's effective segregation coefficient can be used to predict the axial Si concentration in a crystal given an initial melt composition. Also, researchers have previously determined a range of expected dislocation densities for single crystals of SiGe, and a variety of data has been published linking the crystal composition and growth rate to whether the boule is a single crystal or polycrystalline. These results will be used as a yardstick in this work and provide the basis for the test conditions chosen in the following experiments.

2.2.2 Experimental

This work investigates several Czochralski growth parameters and their effect on the macroscopic and microscopic properties of the grown crystal. First, SiGe melts of varying composition will be investigated. As the percentage of Si in the melt is increased, it is expected that several of the deleterious effects mentioned above will be accentuated and degrade the quality of the crystal. In addition, the pulling rate will be varied to determine the limiting growth rate that initiates interface breakdown at the alloy compositions studied in these experiments. Also investigated is the rate of seed rotation and its effect on the constituent microsegregation.

Etchants are utilized to reveal both the solute distribution and the structural perfection of the crystals on a microscale. Wavelength dispersive spectrometry indicates the macroscopic solute distribution within the crystal.

CHAPTER THREE: LITERATURE REVIEW

3.1 Introduction

This chapter discusses previously reported results as a background to the present work. Literature of particular bearing on the present research includes: *(1)* limits on the growth process to maintain single crystalline growth; *(2)* axial and radial binary alloy distribution in crystals grown by the Czochralski technique; and *(3)* lower limits to the dislocation density achieved in previous work.

Temperature stability is crucial for successful Czochralski growth. A cold seed and a hot melt necessarily lead to adverse temperature gradients in the system and to related convection in the melt. A boundary layer between the growing crystal and the melt forms in Czochralski growth, the dimensions of which (δ) is controlled by convection (forced or natural). In order to keep the established solute boundary layer thin and uniform, excellent temperature control coupled with low temperature gradients and slow growth rates appear desirable (7).

In crystal-melt systems, instantaneous control of the microscopic growth rate is not possible through external manipulation of the temperature gradients in the hot zone since a finite time is required to transfer heat over macroscopic distances. Therefore, time-dependent convection can cause difficulties in Czochralski growth, modifying the rate of growth as well as the characteristics of the solute boundary layer. This, in turn, results in changes in the effective segregation coefficient (k_{eff}) which is a parameter that relates the solute concentration in the solid to that in the bulk melt and determines the crystal composition. The observable effect is bands of differing compositions termed "fundamental striations" (4). These are in contrast to "rotational striations" which result when the rotational and thermal axes do not coincide. Therefore, if efforts are not made to eliminate the time dependence of convection, the grown crystal will be composed of bands of material resulting from a series of accelerated growth and remelting sequences.

The dimensions of the striations are dictated by the microscopic rate of growth which, during crystal growth from the melt, is controlled primarily by the transport of heat within the solidification system.

In conclusion, the precise control of the microscopic growth rate and of bulk melt convection is difficult in conventional Czochralski crystal growth systems. Radial and destabilizing vertical temperature gradients in the hot zone can lead to time-dependent convective fluid flows in the melt which, due to their effect on heat and mass transfer, adversely influence growth and segregation. In addition, any imbalance in radial heat input to the melt (thermal asymmetry) causes periodic variations in the microscopic rate of growth and in dopant incorporation if the crystal is grown with seed and/or crucible rotation. Thus it is of fundamental importance to understand the origin and nature of perturbations in growth rate if composition control on a microscale is to be achieved.

3.2 Spatial Distribution of Solute

3.2.1 Use of Heat Pipe

The introduction of a "heat pipe" into the hot zone of growth systems has been shown to be effective in establishing thermal symmetry and in controlling axial and radial thermal gradients in the growth system. Therefore, a heat pipe can be used to minimize thermal convective processes in the melt and their effects on growth.

A heat pipe consists of a double-walled, cylindrical reservoir with a heat transfer fluid such as sodium. The heat pipe is placed coaxially inside the graphite heater of a conventional Czochralski system and coaxially about the crucible containing the molten charge. In this configuration the heat input to the heat pipe along the lower periphery results in the evaporation of sodium (within the confinement of the double-walled tube) and its condensation in the upper (cold) part. Through the absorption of the latent heat of vaporization (lower part of heat pipe) and the release of the latent heat of condensation (upper part of heat pipe), rapid and effective heat transfer is achieved and an isothermal region can be established in the interior (adiabatic) region of the heat pipe (14).

The reduced axial thermal gradients encountered within a heat pipe cavity aid in reducing the driving force for bulk melt convection and tend to stabilize the microscopic growth rate. A properly insulated heat pipe virtually eliminates axial thermal asymmetry, thus resulting in the reduction of rotational and radial segregation inhomogeneities by an order of magnitude (15). However, "reduced" convective melt flows continue to be generated by the unavoidable horizontal and destabilizing vertical heat flow components. The spatial nonuniformity of such convective melt flows may prevent the establishment of a uniform solute boundary layer at the growth interface and thus prohibit radially homogeneous composition during crystal growth (14).

3.2.2 Axial Homogeneity Considerations

Pfann (16,17) conducted some of the initial work in the study of convective versus diffusive transport in the melt. Pfann and Scheil (18) predicted the axial distribution of solute in a crystal assuming plane front directional solidification:

$$C_s = k \cdot C_l \cdot (1-g)^{k-1} \qquad \text{Equation 1}$$

in which C_s is the resulting concentration of solute in the crystal, k is the segregation coefficient, C_l is the original concentration of solute in the melt, and g is the fraction of melt solidified. Equation 1 assumes that diffusion in the solid is negligible and that diffusion in the liquid is complete (there is uniform and perfect mixing at all times). The equilibrium segregation coefficient k_o is the segregation coefficient derived from the equilibrium phase diagram and is a function of the melt concentration (4):

$$k_o = \frac{C_s}{C_l^*} \qquad \text{Equation 2}$$

in which C_s is the concentration of solute in the crystal at the solid-melt interface and C_l^* is the concentration of solute in the liquid at the solid-melt interface (fig 2).

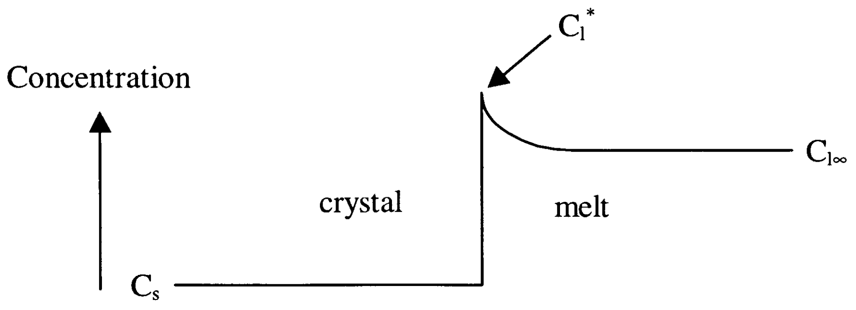

Figure 2. Definition of terms in determining k_o and k_{eff}.

If mass transport is dominated by convective flow, the equilibrium segregation coefficient k_o can be used in equation 1. In reality, though, mass transport is a combination of convection and diffusion processes. In this case, the effective segregation coefficient k_{eff} must be used in equation 1 in which k_{eff} is defined (fig 2):

$$k_{eff} = \frac{C_s}{C_{l\infty}} \qquad \text{Equation 3}$$

in which $C_{l\infty}$ is the concentration of solute in the bulk of the melt (far from the solid-melt interface).

Pfann's treatment of macrosegregation in references 16 and 17 does not treat the initial transient associated with the formation of a solute boundary layer adjacent to the crystal-melt interface (when $k_o \neq k_{eff}$). In fact, though, the rate of diffusion in the liquid is not large enough for the assumption of complete liquid diffusion to be even approximately correct when considering the Czochralski growth of metals.

Burton, Prim, and Slichter modeled the incorporation of solute with consideration of the contribution of solute transport in the melt due to diffusion and fluid motion (19). Their model relates the effective distribution coefficient to the equilibrium distribution coefficient via the boundary layer thickness (δ), the microscopic growth rate (v), and the solute diffusion coefficient (D). To calculate the equilibrium distribution coefficient k_o from the experimentally determined effective distribution coefficient k_{eff}, they propose:

$$k_{eff} = \frac{k_o}{k_o + (1 - k_o) \cdot e^{\frac{-\delta v}{D}}} \qquad \text{Equation 4}$$

The boundary layer δ is a measure of the thickness of a stagnant film in which mass transport is mainly diffusive (20); one growth condition that increases the value of δ is the absence of seed rotation. Small temperature fluctuations at the interface can cause changes in the growth velocity and therefore alter k_{eff} (4,21). One primary goal in Czochralski growth is to keep the boundary layer thickness uniform and constant in order to keep the radial crystal composition constant (4).

Seed and/or crucible rotation forces convection. One beneficial result of seed rotation is that the interface becomes isolated from convective melt instabilities; in addition, seed rotation aids in establishing a uniform solute boundary layer. Both of these characteristics promote uniform dopant incorporation. However, seed rotation can lead to increased radial dopant segregation in the growing boule if the melt is thermally asymmetric in the axial direction. Periodic growth-rate variations can ensue, resulting in rotational impurity striations that are more pronounced than the striations resulting from convective melt instabilities present with no seed rotation (14). Wagner calculates an "effective thickness of the diffusion boundary layer" δ_{eff} (22). He develops three models for segregation: no convection, natural convection, and forced convection via a rotating seed. In his analysis, Wagner accounts for only small (less than 1 at%) concentration variations in the boundary layer. Wagner stresses that concentration differences larger than this can lead to constitutional supercooling and the formation of dendrites; at these higher solute concentrations the linear solidification rate is not directly related to the mass rate of solidification.

Smith expands the work of Tiller to develop a more precise and complete calculation of dopant segregation under various conditions of solidification (23). His mathematical analysis of the distribution ignores convection because, at the time the article was written, it was assumed that natural convection played only a small part in segregation over a wide range of practical conditions of solidification.

Yue and Yue also analyze segregation from a kinetic point of view (24). They formalize a time-dependent solution to axial segregation assuming a constant freezing rate and ignoring the effects of convection. Favier models the rate of solidification as it varies with time in the initial stages of growth (25).

The mathematical treatments of Yue and Yue and Favier are confirmed by experimental results during Bridgman growth of Ga-doped Ge in space (26). In these experiments, Witt reports diffusion-controlled segregation in a microgravity environment. It was found that interface curvature and a time-dependent growth velocity resulted in a segregation profile that differed significantly from the early work cited above.

3.2.3 Literature Values of Segregation Coefficient

For a given melt composition, the equilibrium segregation coefficient k_o determines the crystal composition for conditions without any pile-up of solute at the phase boundary. Therefore, it is an accurate measure of the solute distribution when the solidification velocity is infinitesimally small. According to the phase diagram in figure 3, a binary melt with composition $C_{l\infty}$ will start to freeze when it is cooled to the liquidus temperature. The first solid formed will have the composition given by the solidus line for that temperature ($C_s^{initial}$). But, as melt freezes, the melt is depleted of B in the vicinity of the interface; as a result, the composition of the liquid at the melt-solid interface moves to the left on the phase diagram. The temperature must then decrease for growth to continue. As the concentration of solute (B) in the liquid decreases, the concentration of B in the growing crystal also decreases, approximately following the solidus line. This process continues until the melt is nearly depleted of any solute (C_l^{final}), and therefore the solid also becomes depleted of solute. In principle, the first part of the crystal formed is solute-rich for the phase diagram in figure 3 (k>1), but the concentration of solute in the boule quickly tails off as all of the solute in the melt is rapidly incorporated into the first parts of the growing crystal.

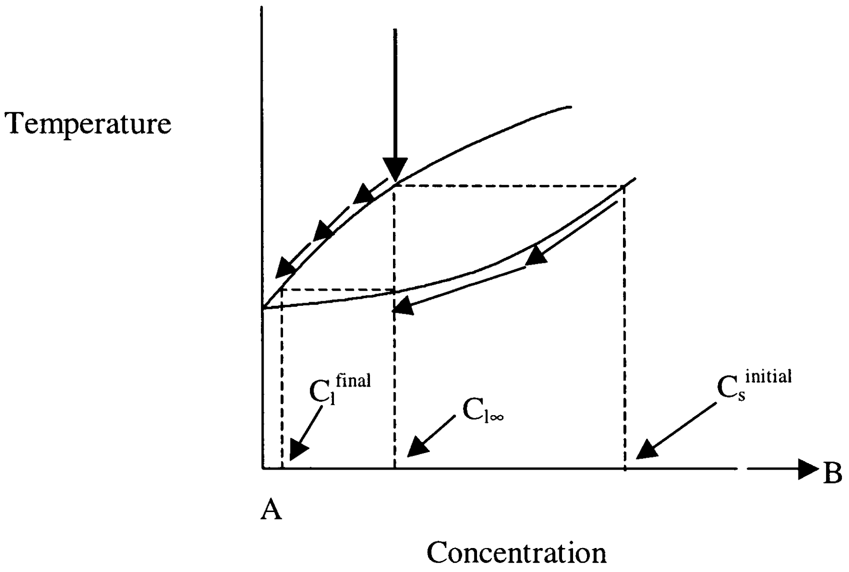

Figure 3. Axial segregation of solute during Czochralski growth.

The effective segregation coefficient k_{eff} is a function of prevailing growth conditions (see equation 4). k_{eff} will equal k_o under the conditions of complete mixing of the melt resulting in the elimination of a solute boundary layer (3). Conversely, for fast growth velocity or conditions leading to a large boundary layer, k_{eff} will go to 1. The SiGe system exhibits values of k_o>>1 and reported values of k_{eff} also much larger than 1. The result is large composition variations in the boule for small changes in growth velocity (4).

The literature indicates a wide variation in reported values for k_{eff} in Czochralski growth and only slight variation in the reported value for k_o for dilute levels of Si in Ge. According to the phase diagram, for 1 at% Ge solute in Si, $k_{Ge} = 0.32$; and, for 1 at% Si solute in Ge, $k_{Si} = 5.25$. Romanenko and Smirnov report values of 1.8, 2.0, and 3.0 for k_{eff} when the melt material is only a few at% Si (27). Helmers reports a segregation coefficient of 2.99 for 15 at% Si in the solid (20). Rouzaud reports $k_{eff} = 4.11$ for 5 at%

Si in the boule (28). Dahlen reports values for the equilibrium and effective segregation coefficients for 2% and 10% Si in the melt (4). For 2% Si in the melt, Dahlen reports k_o = 5.5 and k_{eff} = 4.4; for 10% Si in the melt, the paper reports k_o = 2.8 and k_{eff} = 2.7. Schilz and Romanenko report an effective segregation coefficient of 4.9 for 10 at% Si in the crystal (13). Finally, Yonenaga reports k_{eff} = 6.2 for alloys in which the melt was 0.5 at% Si and the resultant crystal was 3.2 at% Si, and he reports k_{eff} = 6.4 for alloys in which the melt was 2.5 at% Si and the grown crystal was 16 at% Si (29). Obviously, the results in which the measured k_{eff} was greater than 5.25 indicate that the separation between the solidus and liquidus lines in the phase diagram should be greater than the representation given in figure 1 for dilute Si in Ge.

It can be seen that a wide disparity exists in the reported value of k_{eff} for low concentrations of Si in Ge. Several possible explanations exist for the discrepancies. First, the analytical method utilized to determine the Si concentration varied between the research groups. Errors in calibration could account for some of the discrepancy. A melt composition may have been incorrectly calculated due to the formation of oxides, etc. Compositional inhomogeneity may have existed in some of the crystals. Finally, differences in the experimental growth conditions is probably responsible for a majority of the difference in values reported for k_{eff}.

The effect of seed rotation on axial solute segregation must also be considered. Seed rotation imposes a condition that is modeled as a partially-stirred melt. In a partially-stirred melt, it is assumed that the distribution of impurities is diffusion limited in a boundary layer of thickness δ and that perfect stirring exists elsewhere in the melt. For small growth rates and large (> 100) values of the Schmidt number, the solute boundary layer thickness is related to the inverse square root of the seed rotation rate (30):

$$\delta = 1.6 \cdot D_L^{1/3} \cdot \eta^{1/6} \cdot \omega^{-1/2} \cdot d^{-1/6} \qquad \text{Equation 5}$$

in which D_L is the diffusion coefficient, η is the viscosity of the melt, ω is the rate of seed rotation, and d is the density of the melt.

3.2.4 Radial Homogeneity

Radial homogeneity is of concern when growing bulk crystal alloys. Coriell and Sekerka developed a theory to predict the lateral solute segregation associated with a slightly curved (solute boundary layer thickness large as compared to the deviation of the interface from planarity) solid-melt interface (31). Their work assumes no convection in the melt. Later work by Coriell expanded the theory by modeling the lateral solute segregation found in a system with large deviations from planarity at the solid-liquid interface (32). The space-based Bridgman growth of Witt found lateral segregation of several times 10^{18} carriers/cm^3 due to a curved solid-liquid interface (26). Other work by Yonenaga analyzed radial segregation in SiGe alloys. One alloy was grown from a melt of 0.5 at% Si at 2 mm/hr pulling rate, 15 rpm seed rotation, and -2 rpm crucible rotation. Another alloy was grown from a melt of 5.0 at% Si at 1 mm/hr pulling rate, 7.5 rpm seed rotation, and -2 rpm crucible rotation. Both alloys showed a variation of solute of less than ± 3% across the crystal cross-section (29).

3.3 Obtaining Single Crystals

Unique difficulties must be overcome in order to grow non-dilute SiGe bulk alloys via the Czochralski technique when starting with a Ge seed. Ge melts at the lowest temperature of the SiGe system. Therefore, Ge seeds have a tendency to melt back during seeding because the temperature gradient across the phase boundary is not large enough in most Czochralski systems to maintain a cold seed. As a result, pure Ge seeds are limited in Czochralski growth to only a few at% Si in the bulk crystal due to large variations in the melting point of SiGe with composition. In addition, the material freezing out first is of high Si content (k_{eff} for Si in Ge is much greater than one), posing strong lattice mismatch problems (3). Constitutional supercooling in front of Ge seeds can also pose problems during seeding and may lead to polycrystallization.

One reported method to overcome this obstacle when growing Ge-rich alloys is to start with a Ge seed and introduce it to a pure Ge melt. Then, after initial growth has been established, controlled feeding of Si rods into the melt can be initiated to maintain the Si concentration at a desired value (13,33). However, this melt feeding procedure is tedious and difficult to control. On the other hand, when growing Si-rich alloys, seeding problems are alleviated because a seed of pure Si can be used and constitutional supercooling is not an issue. The seed will have a higher Si content than the first part of the crystal grown; this condition is reported to lead to fewer grains developing in Bridgman growth (20).

Several researchers have presented results obtained for Czochralski growth of SiGe. Abrosimov (33) obtained single crystals of Si_xGe_{1-x} with $x=0.1$. Yonenaga (29) has grown a crystal with $0.21<x<0.25$ that was single crystalline for 20 mm in length. The solid then became polycrystalline as the growth proceeded. Yonenaga obtained larger single crystals for smaller values of Si atom fraction. All of the crystals reported above exhibited growth striations. Other Czochralski growth results have been tabulated by Schilz and Romanenko (13) and are presented in Table 1.

3.3.1 Effects of Growth Rate

Constitutional supercooling can develop when the pulling rate is too fast. The term *constitutional supercooling* indicates that the supercooling is due to a change in composition, not temperature. During growth from the melt (for $k_o<1$), the chemical species rejected at the interface always has its highest concentration near the growing crystal and decreases with increasing distance from the interface. This concentration change retards the growth of the crystal and is associated with a reduced freezing temperature in the immediate vicinity of the crystal; using the phase diagram, the equilibrium liquidus temperature of the liquid as a function of distance from the interface

Reference (reference #)	Growth Rate (mm/hr)	Composition (at% Si)	Remarks	Results
Belokurova et al. (34)	102.0	0.7 to 2.0	seed rot. 5 rpm, crucible rot. -10 rpm	single crystal
Selikson (35)	18.0	0.3	seed rot. 5 rpm, crucible rot. -10 rpm	single crystal
Tairov et al. (36)	5.0	5		single crystal
Dolivo-Dobrovol'skaya and Smirnov (37)	30.0	4		single crystal
Tairov et al. (38)	2.5	0 to 15	seed rot. 15 rpm	single crystal
Tagirov (39)	3.0	0 to 15	seed rot. 15 rpm	polycrystal
Dahlen et al. (4)	2.8	8.8	seed rot. 5 rpm	polycrystal

Table 1. Representative SiGe Czochralski growth as tabulated by reference 13.

can be plotted. Given the axial temperature gradient in the melt (determined by the growth conditions), the melt temperature increases from the crystal into the liquid. If the applied temperature gradient is less than required to prevent freezing of the melt ahead of the crystal-melt interface, constitutional supercooling is present in the liquid (fig 4).

A planar interface is unstable as it grows into a constitutionally supercooled melt; any protuberance in the interface will grow at a faster rate than the rest of the crystal. One result is that a redistribution of the solute occurs in the lateral direction. Grooves that are either solute rich or solute poor (dependent upon the value of the segregation coefficient) develop in the growing crystal. Eventually interface breakdown can occur, resulting in polycrystallinity. Constitutional supercooling that resulted in a high degree of interfacial instability is shown in figure 5.

SiGe alloys grown in the <100> direction have a natural tendency to facet due to kinetic supercooling. As a planar interface breaks down due to constitutional supercooling, facet formation is even more probable, leading to the development of hexagonal cells in the boule. It has been found (40) that when Ge crystals are grown from seeds oriented in the <100> direction, the cell faces are the four {111} planes inclined at 54°44' to the plane of the interface. However, various transition structures (dependent upon the growth orientation) often exist before a well-developed cell structure is obtained. First, the transition from a planar to a cellular interface includes a smoothly curved region in which the interface gradually changes from a planar structure to an increasingly undulating interface (40). Then, as summarized by Flemings (41), an unstable interface in

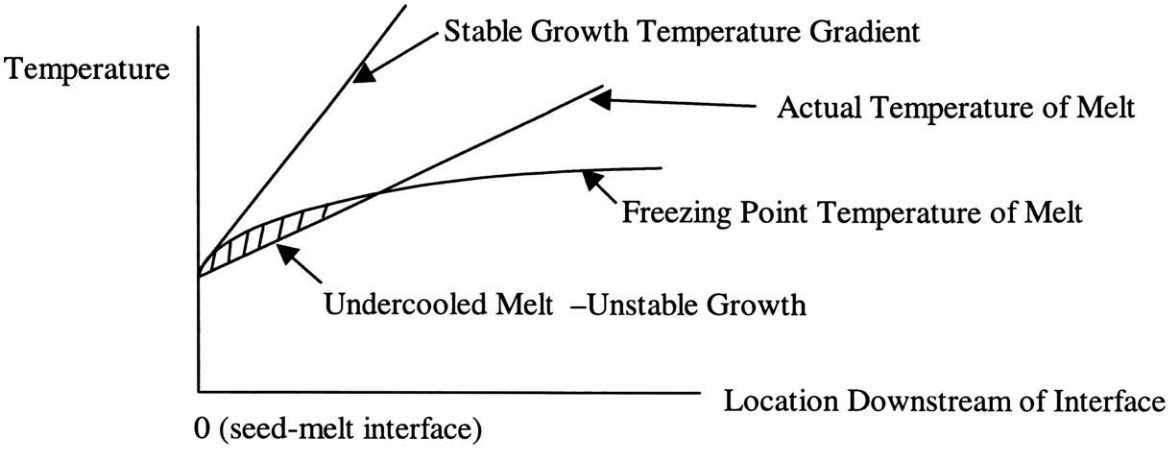

Figure 4. Temperature conditions leading to constitutional supercooling.

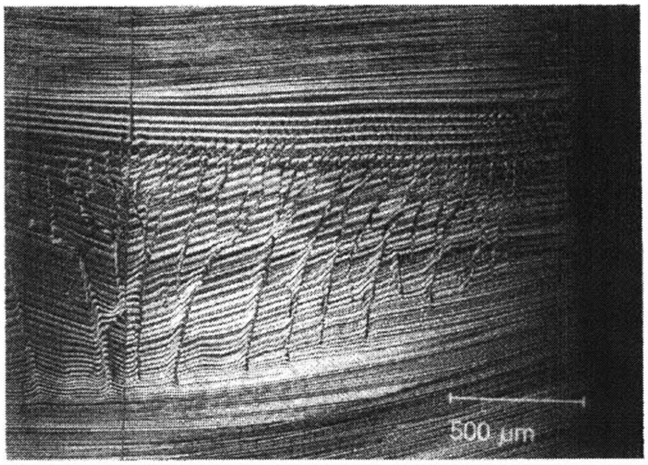

Figure 5. Interface instabilities in SiGe alloy resulting from constitutional supercooling during Czochralski growth. Reference 4

a non-faceting material can take the form of elongated cells or cylindrical nodes. In both cases, the solute segregates in the intercellular regions. When examining the growth of SiGe alloys, the tendency for facet formation further determines the mode of interface breakdown. Given a sufficient fraction of solute, deep-grain boundary grooves can form at solute-enriched locations (fig 6).

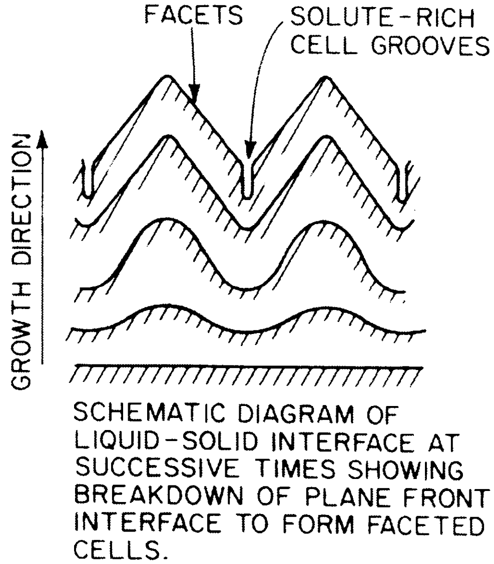

Figure 6. Evolution of interfacial structure due to constitutional supercooling. Reference 41

Values for the length of the constitutionally supercooled zone of liquid adjacent to a growing solid-liquid interface were calculated by Tiller (42). Tiller's analysis removes the assumption of perfect mixing in the liquid. Rather, Tiller assumes that convection in the liquid is negligible, and mixing is due solely to diffusion of impurity in the melt. Tiller quantitatively assesses the case of diffusion-controlled solute transport in the melt for various rates of solidification. The proposed solution to the solute transport equations is found to vary exponentially with the solidification rate.

The Tiller criterion (42) can be used to determine the critical crystal pulling rate below which interface breakdown is avoided:

$$v_{cr} = \frac{D \cdot \nabla T \cdot k_o}{m \cdot C_o \cdot (1 - k_o)} \qquad \text{Equation 6}$$

in which v_{cr} is the critical growth rate, D is the diffusion coefficient for Si in Ge, ∇T is the temperature gradient in the melt, k_o is the equilibrium segregation coefficient, m is the slope of the liquidus curve at the melt composition of interest, and C_o is the concentration of solute in the melt. Growth velocities larger than v_{cr} determined by equation 6 are expected to result in polycrystalline growth. Because of the low diffusion coefficients of the SiGe system, and assuming a temperature gradient of 50 K/cm, the Tiller criterion predicts a maximum pulling rate for single crystalline SiGe growth of only a few mm/hr for alloys of SiGe between 20 and 80 at% Si (3,13). Alloys with either Ge or Si in excess of 80 at% have larger calculated critical growth velocities in the range of 1-5 mm/hr (13).

However, the pulling rate should continuously be adjusted during growth since the melt composition continuously changes in an isolated Czochralski system and is a function of the melt volume. Only by controlling the pulling rate can a constant crystal diameter be maintained and supercooling in the melt avoided (9). In the SiGe system, the decrease of Si concentration as growth progresses is accompanied by a slowing of the growth velocity. If the pulling rate remains constant, the melt region ahead of a Ge seed can become constitutionally supercooled (20). Unfortunately, though, it is not possible to continuously and directly measure the melt temperature at the solid-melt interface when growing a device-quality crystal.

3.3.2 Lattice Mismatch and Resulting Stress

Experiments show (fig 7) that the lattice constant for SiGe alloys can be closely approximated by taking a linear interpolation between the lattice constants of pure Si and Ge (in other words, Vegard's law is a good approximation of the lattice constant) (1,7):

$$a_{Ge_xSi_{1-x}} = a_{Si} + (a_{Ge} - a_{Si})x \qquad \text{Equation 7}$$

in which a_{Ge} = 5.658 Å, a_{Si} = 5.428 Å, and x is the mole fraction of Ge in the SiGe alloy. In epitaxial growth, when SiGe layers are deposited on Si substrate, the maximum lattice mismatch is 4.2% (43).

This mismatch of lattice parameters results in mechanical stresses in the contact area between the seed and the melt (33). In Czochralski growth, lattice mismatch between the seed and the equilibrium concentration transients in the crystal corresponding to the varying microscopic growth rates can lead to polycrystalline growth (4). One way to decrease the lattice mismatch is to increase the pulling rate (which produces a more homogeneous material). However, the desire to reduce the lattice mismatch via fast pulling is in conflict with the slow pulling rates needed to avoid constitution supercooling. Therefore, a balance must be achieved.

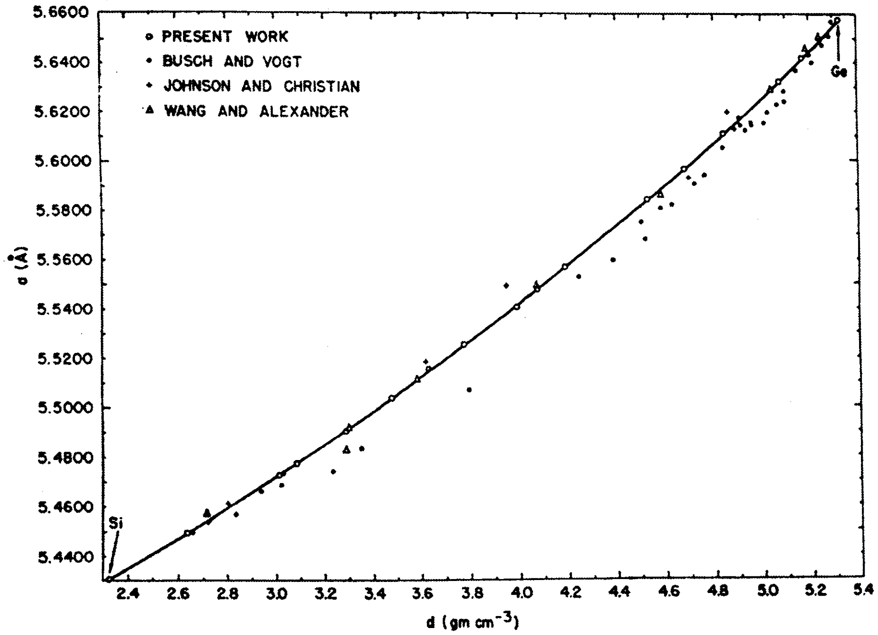

Figure 7. Lattice constant as a function of composition for the Si-Ge system. Reference 1

One reported method of reducing the mechanical stress induced by lattice mismatch is accomplished by ramping up the percentage of Si in the seeds through a series of growth processes (13). An alloy of SiGe is grown with a low percentage of Si that allows the crystal to remain single crystalline. A portion is cut from the crystal to become the seed for the next growth experiment. The process is continued with increasing amounts of Si in the melt to produce the final desired crystal composition. Another option is to continuously feed Si rods into the melt at a rate faster than the incorporation of Si into the growing crystal. This method is more amenable to large melt volumes and imposes additional hardware requirements.

3.4 Dislocation Density

3.4.1 Introduction

Compositional fluctuations necessarily cause variations in an SiGe alloy's lattice constant. This causes strain in the boule that must be relieved, and if the strain is large enough dislocations are formed. The density of dislocations in the grown crystals is of critical concern when attempting to produce a device-quality crystal. It has been estimated that a striation producing a concentration step of only 0.1 at% Si will produce a linear dislocation density of approximately 1000 dislocations/cm parallel to the striation (13).

3.4.2 Types of Dislocations

Because of the variety of dislocations present in materials (edge dislocations, screw dislocations, and combinations thereof), dislocation pits of unique nature can be detected in a boule for a given etchant. The appearance of etch pits has been summarized by Ellis (44). When using an etchant composed of dilute, chlorinated KOH, Ellis observed three types of etch pits. First, there are relatively large etch pits which result from edge dislocations. This type of dislocation is common in crystals grown in the <100> direction, but they are much less prevalent in <111> grown crystals. These etch pits can align themselves to become more thermodynamically stable, forming small-angle grain boundaries. Etch pits with spiral terraces can also often be detected in etched boules. The spiral structure of the pit denotes a dislocation with a large screw component. The pitch of the terrace structure is an indication of the magnitude of the Burgers vector and its orientation to the free surface.

3.4.3 Radial Variation of Dislocation Density

As the center of a crystal is more inert against temperature changes than the periphery, the amplitudes of striations are usually lower, which leads to lower defect densities in the center of the boule. Typically the etch pit density in the radial center of the crystal is one or two orders of magnitude lower than on the periphery (13). SiGe solid solution single crystals reported in the literature have shown etch pit densities ranging from $10^2/cm^2$ (in the center of the crystal, where the interface is nearly planar and the region undisturbed) to $10^7/cm^2$ (near the edges of the crystal) (4,7,13,29).

CHAPTER 4: EXPERIMENTAL CONDITIONS

4.1 Introduction

This chapter describes the hardware used in the present work, the general procedures for crystal growth, and the analytical techniques used to characterize the crystals grown.

4.2 Experimental Apparatus

A traditional Czochralski pulling system was used to grow the SiGe crystals analyzed in this research (figs 8 and 9). The growth system consisted of a double-walled stainless steel chamber [A]. The chamber was separable into two pieces, allowing access to the heating components within the body. Both the top and bottom halves of the body were continuously fed with chilled water to keep the stainless steel walls cool throughout the growth process. A needle valve attached to the top half of the body allowed a supply of argon gas, while an exit port on the other side of the pulling body was attached to a needle valve that controlled the exit velocity of the inert gas. The argon was bubbled through a glycerin reservoir upon exiting the system, allowing the inert gas pressure to be monitored and maintained at approximately 4 psig overpressure throughout the growth process. Another port in the chamber body allowed for a pressure gauge to be attached to the system.

The top part of the chamber had a 66 mm diameter viewing port to allow visual observation of the crystal-melt interface. The seed shaft [B] slid through the top of the chamber body through a double O-ring assembly that tightened around the shaft as a brass cap [C] was screwed to the top of the chamber body. The brass cap also contained a series of ten teflon chevrons that tightened around the seed shaft as the cap was tightened. The teflon chevrons ensured a tight seal with the shaft while still allowing the shaft to rotate.

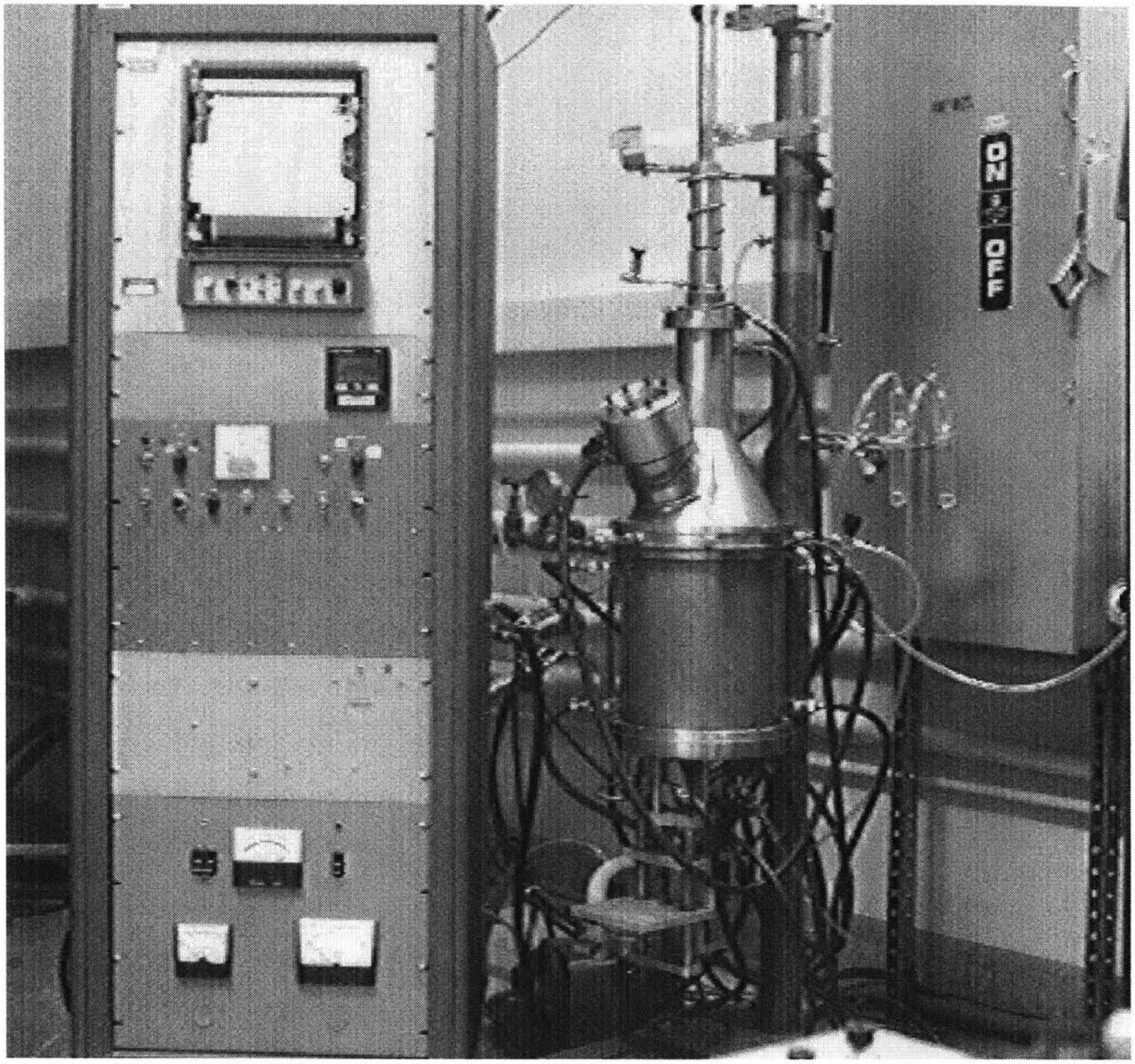

Figure 8. The Czochralski puller used in this work.

The chamber body also had a double O-ring assembly on the bottom plate to allow the crucible shaft [D] to slide up and down. The crucible shaft height could be adjusted 115 mm vertically by a screw assembly below the base plate of the chamber. Two isolated electrical contacts [E] were located on the outside base plate of the chamber, feeding the current to two electrode ports that protruded 24 cm into the body of the chamber.

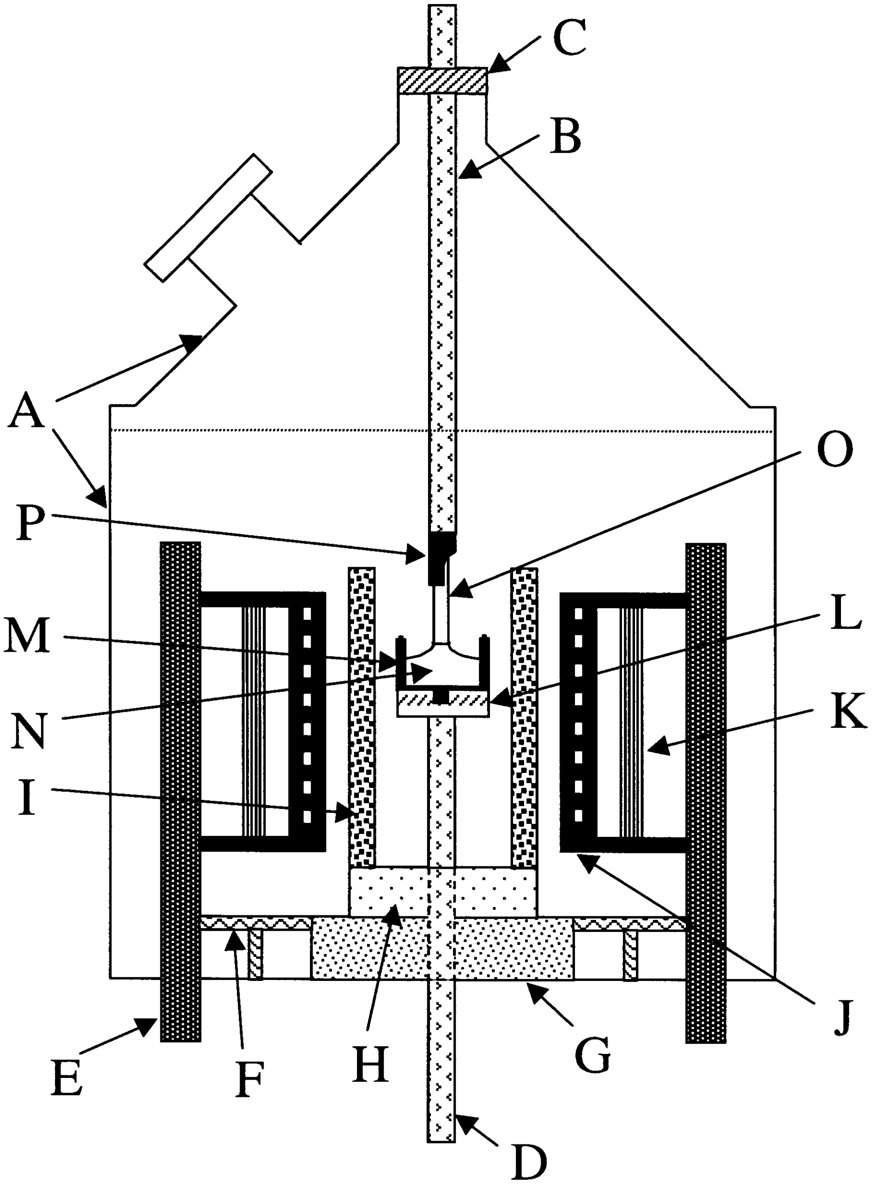

Figure 9. Schematic of the Czochralski device chamber body.

(a) Furnace

The components of the heating system could be removed in order to clean the inside of the chamber. Two molybdenum plates [F] standing 40 mm above the base of the chamber functioned as heat reflectors. A graphite block [G] 40 mm tall rested on the bottom of the chamber and had a hole cut in the middle to allow the crucible shaft to pass through. On top of the graphite block rested an insulating stand composed of lava [H]. An inconel heat pipe [I] with sodium as the heat transfer medium rested on top of the lava stand. The heat pipe was 15.24 cm tall, 39.6 mm i.d. and 73.2 mm o.d. The heat pipe was centered coaxially about the crucible. A graphite heating element [J] encased the heat pipe. The ladder-type heating element was 14.07 cm high and 76.2 mm i.d.; it was composed of 46 connected horizontal "slots" of graphite each 1.59 mm wide. The heating element was machined from 2020 grade graphite (Union Carbide Specialties). It was secured on top and bottom by stainless steel clamps that were isolated from the furnace and attached to each of the electrode ports with set screws. Approximately 35 volts were required to pass 30 amps of current through the graphite element at the operating temperature for growth. It yielded a growth temperature in the heat pipe of 975 °C. A corrugated nickel heat shield [K] was positioned around the graphite heating element in order to reduce heat losses to the furnace walls. A chromel-alumel (type K) thermocouple measured the temperature in the heat pipe 32 mm deep (from the top of the pipe) midway between the inner and outer diameters of the heat pipe. The temperature recorded from this thermocouple fed a PID (proportional, integral, derivative) controller that maintained the temperature at a value set by the user by controlling the current flowing through the device. The PID controller stabilized the nominal temperature at ±0.1 °C.

The inconel crucible shaft (18.7 mm o.d.) could be raised between 7" and 11.5" above the inside floor of the chamber. A graphite mating piece [L] was attached to the top of the crucible shaft and a tight fit was maintained by using graphoil tape. The crucible [M] (either graphite or quartz) then sat upon the mating piece, again using graphoil tape to provide friction. Both the graphite mating piece and crucible were machined from 2020 grade graphite. The quartz crucibles were made from GE-214 quartz. The crucibles had an inner diameter of 31 mm, an outer diameter of 35 mm, and an interior height of 20 mm.

Ge melts are traditionally contained in graphite crucibles since pure Ge does not wet carbon. However, it only takes about 1 at% Si to cause the melt to stick to and react with a carbon vessel (forming SiC). An alternative crucible material is pyrolytic boron nitride. This material has a high degree of chemical inertness; but, boron will leave the crucible material and contaminate the melt, resulting in p-type crystals with a density of electrically active impurities of approximately $10^{16}/cm^3$ (13). Another option is to use quartz crucibles when Si is in the melt. Therefore, a graphite crucible was used in the initial growths of Ga-doped Ge. Then, growth of SiGe alloys was attempted in a graphite crucible. As detailed below in the experimental results, though, a surface film formed when a graphite crucible was used. As a result, quartz crucibles had to be used when growing SiGe alloys.

(b) Crucible and Charge

The Ge and Si charge material [N] were etched in CP4 (70% HNO_3 : CH_3COOH : 48% HF in 5:3:3) for 2 minutes at room temperature. X-ray fluorescence revealed that the Ge was doped with Ga ($\sim10^{17}/cm^3$) and had no other elements above minimum detection levels ($5x10^{18}/cm^3$). Electronic grade (99.9999%) Si was used in the melt. For the Ga-doped Ge crystals, the Ga dopant (99.999%) was not etched. After etching, the charges were immersed in deionized water and rinsed with acetone before being blown dry with a stream of purified nitrogen. Prior to filling the graphite crucible with the charge, the inside of the crucible was wiped with a lint-free cloth to expose a new graphite surface, and any resulting graphite dust was blown out of the crucible with compressed air.

(c) Seeds

Ge seeds 4 mm by 4 mm by 4 cm were cut from a large boule of material that had been previously grown by the Czochralski method. The seed material was Ga-doped to $5x10^{19}/cm^3$. Etching revealed that the seeds had a high ($\sim10^4/cm^2$) density of dislocations. Laue back reflection measurements confirmed that the seeds were oriented to within 2° of the desired crystallographic orientation <100>. The seed [O] was secured in a graphite seed holder [P] by three independent loops of wire that rested in grooves filed into the sides of the seeds. The seeds were etched in CP4 for 2 minutes. The graphite seed holder was then attached to the stainless steel seed shaft. The seed shaft was connected to a lifting and rotation system. Variac speed controllers maintained the desired growth parameters. The seed shaft could be raised/lowered over 55.9 mm. A rubber, vibration-damping connector isolated the seed shaft from the seed rotation motor assembly.

4.3 Growth Procedures

Prior to growth, the chamber was cleaned with acetone and wiped with Kimwipes tissues. The chamber was then brought under vacuum for several hours to ensure all solvents had outgassed from the interior.

After opening the furnace, the graphite crucible mating piece and the crucible containing the charge materials were attached to the crucible shaft. Minimal thermal asymmetry results when the heat pipe is perfectly aligned about the crucible. Therefore, the heat pipe was centered about the crucible with a feeler gauge (clearance of 2.3 mm around the crucible). The top half of the chamber was mated to the bottom half utilizing an O-ring lubricated with high-vacuum grease; this provided a tight seal between the two pieces in both vacuum and over-pressure situations. Three bolts secured the two chamber pieces together. The seed holder was secured to the seed shaft, and a thin film of vacuum oil was applied to the seed shaft to aid in lubricating and sealing with the teflon O-rings. The seed shaft was secured with the brass cap loosened just enough to allow the seed shaft to rotate. The entire assembly was then brought under vacuum (< 500 mtorr) to verify that minimal leaks were present in the system. The chamber was alternately filled with argon gas overpressure and evacuated three times to ensure any residual gases in the chamber were removed. The cycles were completed with the device under positive pressure with argon exiting the device through the glycerin reservoir.

Cooling water was turned on; the water maintained the outside of all the stainless steel walls at room temperature or colder. The crucible was lowered 7 cm deep into the heat pipe and power to the heater was turned on. The temperature in the heat pipe was raised

150 °C every ten minutes until the temperature reached 920 °C. The temperature was then raised in increments of 10 °C until the charge material melted. The crucible was raised to approximately 1 cm below the top of the heat pipe. This position had proven to have the optimum axial temperature gradient for growth. The temperature in the heat pipe was then decreased 5 °C to ensure that the charge material began to crystallize at that temperature. The charge material temperature was then increased 3 °C to obtain the final growth temperature. The seed was lowered to within 1 cm of the melt and maintained at that height for 15 minutes to achieve thermal stability.

Seed rotation was started at the operating rate (15 or 20 rpm) for the test. The seed was lowered to the surface of the melt and then the seed was raised at approximately 40 mm/hr after a stable interface had been established. Initial "fast" removal of the seed ensured a small shouldering angle, which allowed twins in the material to propagate to the free surface. The pulling rate was then decreased gradually to the desired steady state pulling rate, forming the necked region of the crystal. Once the desired crystal diameter had been obtained, the temperature of the melt was increased to shoulder the crystal and achieve constant diameter growth. The seed was pulled at a steady rate for the duration of the growth process. Upon completion of growth, the crystal was suspended directly above the hot crucible and any remaining melt material for 15 minutes to avoid thermal shock. Seed rotation was ceased and the crystal was slowly raised from the heating assembly over the course of another 15 minutes. The crucible was lowered down to the middle of the heat pipe to ensure that if any charge material did remain in the crucible, the material would solidify from the bottom up and not crack the crucible. The heater temperature was ramped down over the course of two hours for eventual removal of the grown crystal and any remaining charge material.

4.4 Preparation of Crystals for Analysis

A photo was taken of the grown crystal while still in the seed holder. The crystal was visually observed for the four-faceted structure indicative of a single crystal grown in the <100> direction, and any externally visible boundaries in the material were denoted.

The boule was mounted on a chalk block with Crystal Bond, an acetone-soluble bonding compound (Ciba Products Company, araldite 6060), for the series of cuts to ensue (fig 10). The first cut was made perpendicular to the growth direction to remove the seed from the crystal (cut 1). The cut was made with a wire saw. The abrasive solution used in this process was composed of 600 grit SiC powder suspended in light oil. All remaining cuts were made with a wheel saw (South Bay Technology Inc., model 660) using a seven inch diameter diamond impregnated blade. South Bay Technology Inc. water-soluble coolant (diluted with water 30:1) was used as the coolant during the cutting process. The series of cuts to follow varied somewhat from boule to boule dependent upon the features found in the grown crystal and the need to clarify certain characteristics within each crystal. Generally, first an "axial slice" was cut from the center of the crystal along the growth direction (cuts 2 and 3). The axial slice measured approximately 1 mm in thickness. Then, two disks were cut perpendicular to the growth direction: one at the beginning of growth (hereafter referred to as the "seeding region disk," cuts 4 and 5) and one near the end of growth (hereafter referred to as the "bottom end disk," cuts 6 and 7). These "transverse disks" were cut in order to determine radial properties of the crystal. Each disk was 1 mm thick. The axial slice was analyzed by etching and electron beam microprobe analysis, while the transverse disks were analyzed only by etching. All slices cut from the boule were removed from the cutting block by slightly warming the crystal to loosen the Crystal Bond. Immersion in acetone then removed any residual Crystal Bond from the slices. Usually the axial slice had to be cut into two pieces because it was larger than the brass polishing disks (34 mm diameter).

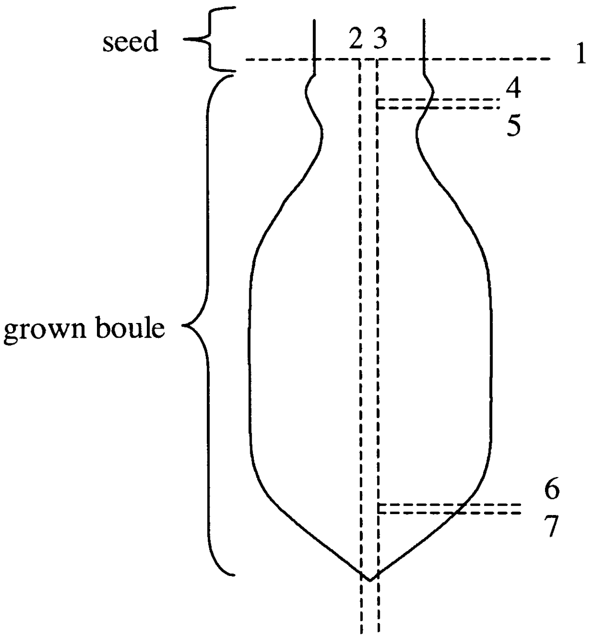

Figure 10. Typical cutting scheme in preparation of boule analysis.

The slices were washed with soap and deionized water to remove any residual abrasives from the cutting process. All slices were individually mounted on brass disks with the bonding compound. The polishing disk was then attached to a hand-held stainless steel chuck. Each piece was lapped for approximately 20 minutes to remove saw damage and to produce a flat face. The lapping solution consisted of 3 μm iron oxide powder mixed with deionized water to form a slurry; lapping took place on a glass plate. The samples were then washed again to remove all lapping abrasive. In turn, each brass disk was then secured to a stainless steel polishing wheel and the sample polished with a solution of Syton HT-30 (colloidal silica): H_2O : 30% H_2O_2 in the ratio 200:200:5. Typical polishing times were on the order of one hour. At the conclusion of the polishing process, the slabs were cleaned for one minute with a stream of DI water introduced just ahead of the polishing jig. This rinse prevented any residual polishing solution from crystallizing on the sample.

4.5 Characterization Processes

4.5.1 Etching Procedure

The two transverse disks cut perpendicular to the growth axis were etched to determine the crystalline structure of the grown crystals. The disks were examined under a microscope for the presence of grain or twin boundaries, and also to quantify the dislocation density running in the axial direction. The disks were etched for 15 seconds at room temperature in a solution of 40% HF : 70% HNO_3 : CH_3COOH in the ratio 1:1:1.

Etching was also performed on the axial slice. The slice was preferentially etched to allow for the study of concentration variances via interference contrast microscopy. Concentration variances were detected in the form of striations, solute trails, etc. The alloys were etched for 15 seconds at room temperature in an agitated solution of 40% HF : CH_3COOH : 30% H_2O_2 in the ratio 1:1:1.

4.5.2 Electron Beam Microprobe

4.5.2.1 Introduction

Electron beam microprobe analysis was conducted to determine the composition of each grown crystal at various axial and radial locations. Electron beam microprobe analyses were carried out by wavelength dispersive spectrometry (WDS). For this study, a 15 kilovolt electrical source was used to produce the high-energy electrons that would illuminate the sample. As a result of the incident electrons hitting the sample, X-ray photons of characteristic wavelength were emitted by each element in the sample, and these emitted photons were counted. For Ge, the characteristic wavelength detected was 10.436 Å (Lα) and for Si 7.1254 Å (Kα) was measured. The vacuum level in the apparatus was 10^{-6} torr. The sampling size of the electron beam was a 1 μm diameter circular cross-section, so the technique was amenable to mapping the composition profile in the crystal.

4.5.2.2 Procedure

For each boule, the axial slice in the seeding region was analyzed at 10 μm intervals down the central axis of the crystal for 40 points. Ten of these points were taken in the seed and 30 of the points were in the first part of the grown boule. The remaining portion of each axial slice was analyzed at 1 mm intervals down the central axis of the crystal. Each crystal was also analyzed radially at 250 μm intervals at the halfway point or higher in the growth process (fig 11).

First, Ge and Si elemental standards were each individually analyzed. They provided a reference count of X-ray photons emitted by the pure elements given the specific device conditions. The standards were each analyzed for 40 seconds in two different locations and the characteristic photon count averaged. The difference in reference counts was never greater than 0.15% for the Si and no greater than 1.00% for the Ge. Also, the standards were sampled over a larger cross-section (10 μm diameter circle) than the experimental boules to ensure an average value was collected for the standard reference count. Each grown crystal was then analyzed. Because Ge was present in the alloys at such large concentrations, the Ge characteristic wavelength was counted for only 8 seconds. The Si measurement was conducted for 120 seconds due to its low concentration in the alloy.

The emitted photons for each of the two constituents were counted by a software program that also took into account interference between the elements in the alloy. The counts in the sample were compared to the counts from the two standards to determine the concentrations of Ge and Si in the sample. The output was presented both on an absolute scale and a normalized scale in which the constituents added up to 100.0 at%.

The sum of the absolute values for Ge and Si was always within 0.75% of the expected 100% total (normalized) value. The normalized values are reported in this work.

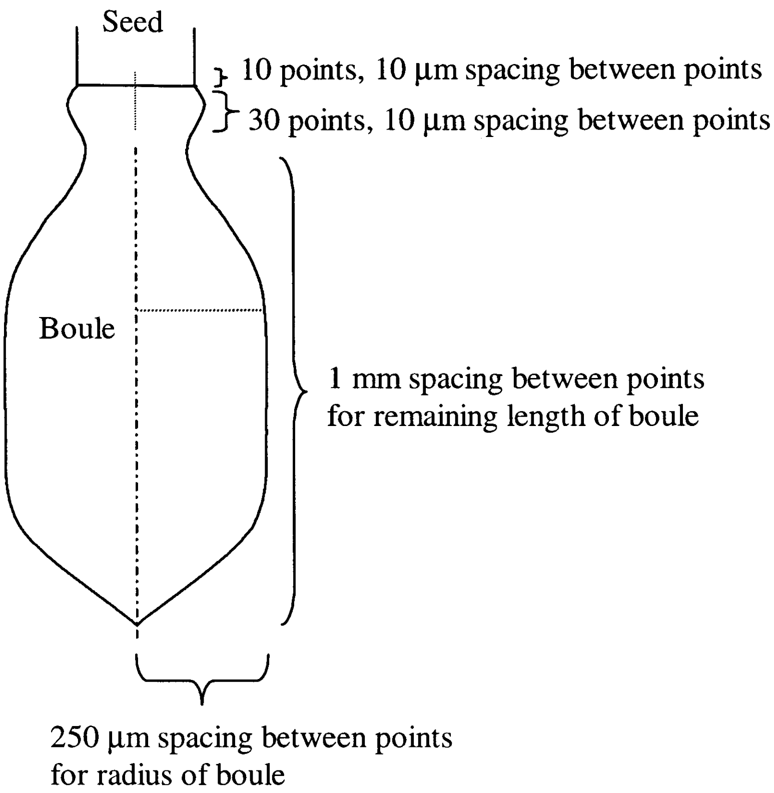

Figure 11. Schematic of sampling scheme during WDS data acquisition.

CHAPTER 5: EXPERIMENTAL RESULTS

5.1 Introduction

Two Ga-doped Ge crystals were grown to serve as standards and to establish growth and characterization procedures. The features of interest in SiGe were analyzed in the Ga-doped Ge standards in order to provide a basis to compare results with SiGe alloys. All of the boules were analyzed for crystalline structure, micro- and macrosegregation of the solute, and dislocation density. The two Ga-doped crystals were analyzed only by the etchants discussed earlier. Four SiGe crystals grown during this study were analyzed by etching as well as by electron beam microprobe (WDS). Several of the boules reveal poor diameter control during the growth process. The variation in diameter results in a range of growth velocities within a single boule.

5.1.1 Synopsis of Results

Section 5.1.1 provides an overview of the results found from the four SiGe crystals grown in this work. Sections 5.2 and 5.3 provide more detailed analysis and individual observations from the two Ga-doped Ge and four SiGe growth experiments. Table 2 provides data specific to the growth parameters of each experiment.

5.1.1.1 Structural Perfection

Single crystalline growth occurred for less than 1 at% Si in the boule. The single crystals exhibited low-angle grain boundaries (polygonization) as well as twin boundaries. In addition, other indications of interface instability existed such as "wavy" striations and the formation of solute trails. Finally, two of the growth experiments showed faceting along {111} planes at the initial seed-melt interface.

5.1.1.2 Segregation

5.1.1.2.1 Macrosegregation

As shown in figure 12, the average value for k_{eff} found in this work was 2.75. The Si concentration was effectively constant in the radial direction for the single crystals grown in this work. The polycrystals exhibited a variation in Si concentration radially, indicating that the incorporation of Si at the seed-melt interface appears to be sensitive to the crystallographic orientation of the growing crystal.

Coriell's theory in references 31 and 32 describes the effect of a curved interface on the radial segregation of solute in the crystal. A curved interface causes nonuniformity in the solute boundary layer; the result is variation in the rate of solute diffusion at different radial locations. However, Coriell's theory assumes diffusion-driven growth with negligible convection in the melt. Therefore, Coriell's theory is not applicable to this work, since the immediate growth of the boules at maximum Si concentration (described below) indicates a very shallow solute boundary layer for these experiments. The shallow boundary layer could be due either to fast indiffusion of the solute or strong convection in the melt. Regardless of the cause, a thin solute boundary layer results in little radial segregation of solute in the crystal (as observed in this work).

5.1.1.2.2 Microsegregation

Rotational striations appeared in all of the crystals grown. In every crystal, the striations were easily identified near the edge of the boule. However, in the middle of the boule, the striations gradually faded and were not identifiable. This effect is attributed to the curvature of the solid-liquid interface. Near the edge of the boule, the curvature of the interface causes the growth velocity to fluctuate as the boule is rotated and slowly pulled out of the melt. It is the fluctuation in growth velocity that causes the microsegregation to occur which is evident as striations. Near the middle of the boule, though, the solid-liquid

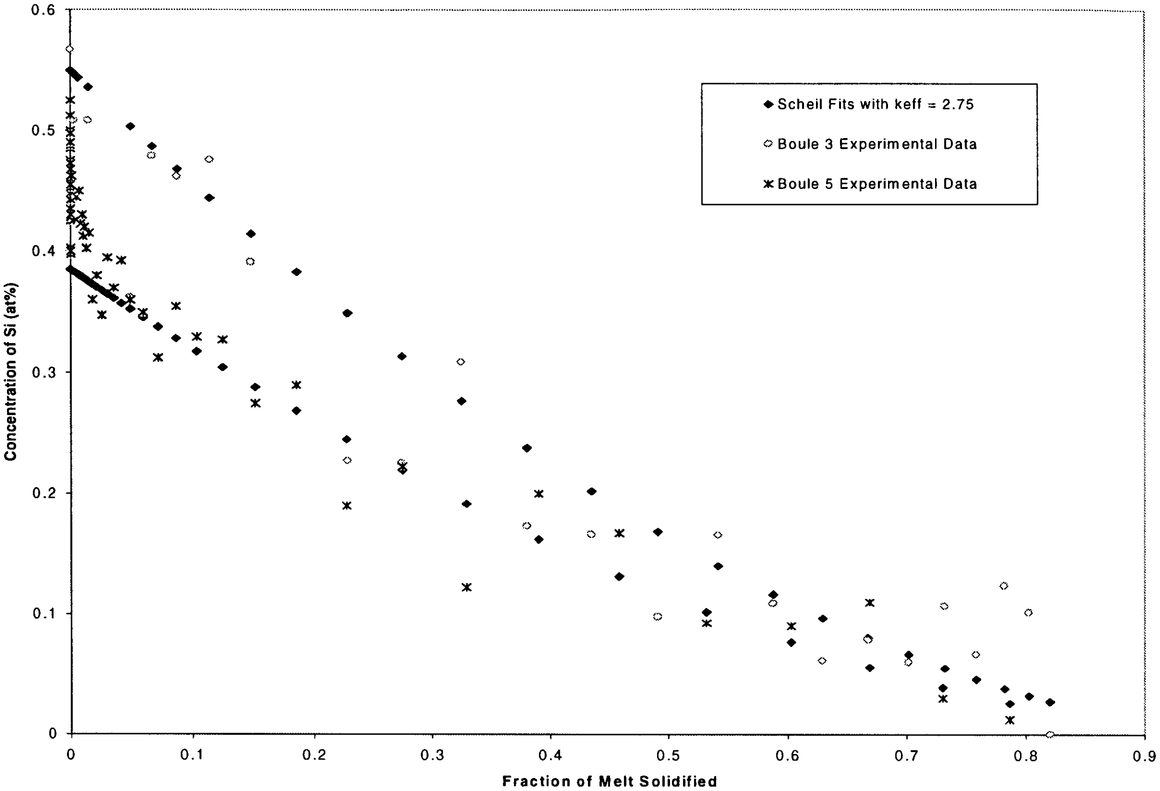

Figure 12. Scheil Fit (k_{eff} = 2.75) plotted with the experimental results from boule #3 and boule #5.

interface is nearly planar and therefore one steady growth rate exists. The result is the absence of rotational striations in the middle of the boule (assuming there is no precession of the seed during growth).

The variation of the lattice constant within a rotational striation can be predicted. For this work, in which the melt concentration was ~0.25 at% Si and k_{eff} ~ 3, 0.75 at% Si is the expected solute concentration in the growing crystal. Now, if this 0.75 at% Si material melts back during a rotation of the boule and forms a layer of 0.75 at% Si in the melt at the crystal-melt interface, a rotational striation of 2.25 at% Si is expected to form during regrowth (still assuming k_{eff} ~ 3). The melt layer will quickly be depleted and normal growth of 0.75 at% Si will then resume. Therefore, from Vegard's Law, the rotational striation has a lattice constant 0.0035 Å (0.06%) smaller than the surrounding crystal material, forming tensile stress within the rotational striation.

Crystal	Weight Ge (g)	Weight Ga/Si (g)	Initial Melt Composition	Crucible Material	Ar Overpressure (psig)	Growth Temperature (°C)	Pull Rate (mm/hr)	Growth Rate (mm/hr)	Max Si Conc. (at% Si)	Measured k_{eff}	Results
Boule 1 (GaGe)	52.0623	0.0400	3.5×10^{19} Ga atoms per cm^3	Graphite	4	978.5	3.9	5.5			Single crystal
Boule 2 (GaGe)	65.0328	0.0816	5.8×10^{19} Ga atoms per cm^3	Graphite	4	985.5	8.6	13.3			Single crystal
Boule 3 (SiGe)	51.5480	0.0474	0.24 at% Si	Quartz	4	984.0	3.2	3.7-9.1	0.57	2.5	Single crystal
Boule 4 (SiGe)	70.0335	0.0841	0.31 at% Si	Quartz	4	979.0	2.9	3.8	0.58		Cold-seeded; polycrystal
Boule 5 (SiGe)	44.4951	0.0404	0.23 at% Si	Quartz	4	972.5	2.9	7.5-11.0	0.51	3.0	Single crystal
Boule 6 (SiGe)	30.5772	0.3965	3.2 at% Si	Quartz	4	998.5	5.9	20	3.43		Polycrystal

Table 2. Growth conditions for this work.

X-ray diffraction measurements within a rotational striation possibly could detect this variation in the lattice constant (strain broadening of the peak), and then an internal stress could be calculated from the measured lattice constant. However, surface preparation would be difficult, as work-induced stress could mask the stress due to the variation in lattice constant. Annealing could possibly reduce the work strain to acceptable levels for an accurate measurement of the lattice constant and therefore the internal stress in the rotational striation, but this process was not performed in this work.

Fundamental striations were not visible in any of the boules grown in this work. This could be due to rapid mixing in the melt, forming fundamental striations of low Si concentration. The etchant used in this work may not have been sensitive enough to detect the relatively low Si concentration differences. Or, the resolution of the microscopy in this work (~3 μm) may not have been high enough to detect the fundamental striations.

5.2 Ga-Doped Ge Standards

5.2.1 Boule #1

The goals of this growth experiment were to become familiar with the Czochralski growth system and establish growth standards by which all subsequent processes were analyzed by comparison.

Initial dopant concentration of Ga in the melt was adjusted to obtain $3x10^{18}$ Ga atoms/cm^3 at the beginning of the growth process assuming a distribution k_{eff} of 0.087 (45). The steady-state region of interest was grown at 5.5 mm/hr, and the seed rotation rate was 20 rpm (no crucible rotation was applied in any of the experiments). The dimensions of the steady-state region were 16 mm long and 17 mm in diameter. The entire crystal measured 57 mm in length and varied between 17 and 22 mm in diameter except for the beginning and end of the growth process (fig 13).

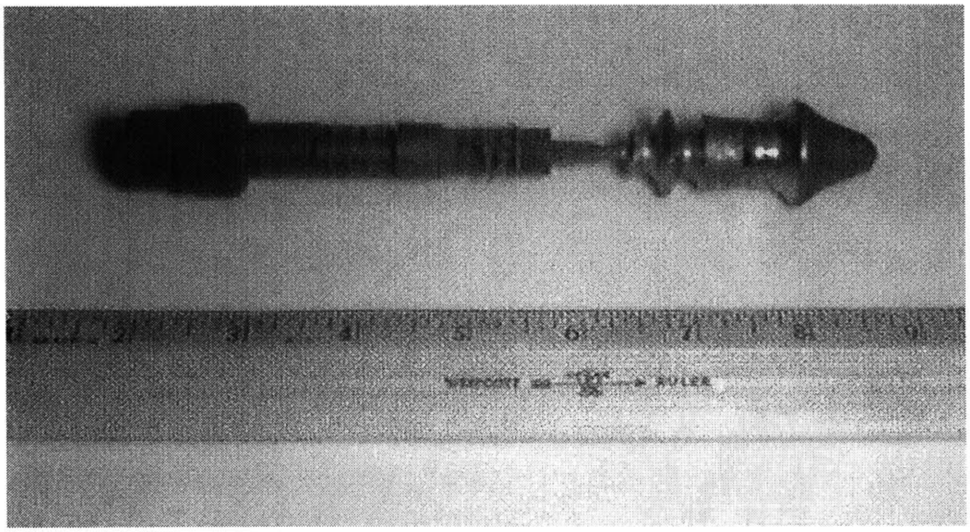

Figure 13. Boule #1 (Ga-doped Ge).

5.2.1.1 Crystallinity

Visual examination of the morphology of the crystal indicated it to be "single" crystalline for nearly the entire growth process. All of the crystals grown in this work were grown in the <100> direction. This boule had four distinct external facets oriented at 90° to each other evident over virtually the entire length of the boule (disappearing only at the very beginning and end of the growth process).

The crystal was cut as described in section 4.4. Observation of the axial slice of the boule indicated two twins originating in the seed material propagated into the grown boule. Also, several formations of aligned dislocation pits were found in the crystal propagating parallel to the growth direction. The lines of dislocation pits are assumed to be low-angle grain boundaries and will be referred to as such in the remainder of this work. However, these aligned dislocations could reflect residual work damage on the crystal surface. Therefore, even though this material is termed "single crystalline," there were boundaries of misoriented lattice structure separated by low-angle grain boundaries. The low-angle grain boundaries never did reach the surface of the boule; as a result, the external morphology appeared single crystalline.

5.2.1.2 Distribution of Solute

After performing preferential etching on the axial slice, rotational striations were observed via interference contrast microscopy. The measured striation separation was 5.0 μm with a standard deviation of 0.8 μm (fig 14). The (measured) upward displacement of the pulling rod for steady-state growth was 16 mm. Given a crucible diameter of 3.1 cm and a boule diameter of 17 mm, an additional 5 mm of growth must be attributed to the lowering of the solid-liquid interface during this period of growth for a total growth length of 21 mm. Growth occurred at 20 rpm seed rotation over the course of 213 minutes, which corresponds to an expected rotational striation separation of 4.9 μm/striation.

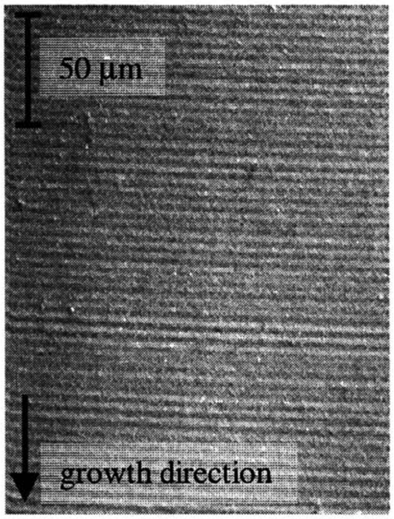

Figure 14. Rotational striations in boule #1.

5.2.1.3 Dislocation Density

Upon etching, both the upstream and downstream transverse disks exhibited several low-angle grain boundaries composed of densely-packed dislocations. The low-angle grain boundaries in the boule had an average linear density of 1250 dislocations/cm (fig 15). Also, additional dislocations occupied 25% of the surface area and were located on just one side of each disk. Their highest density in this region was $2.5\text{x}10^3/\text{cm}^2$. In the axial slice, a few dislocations were apparent for only the first cm of growth. The dislocations then apparently oriented parallel to the growth direction, eliminating any etch pits from the axial slice in later growth periods.

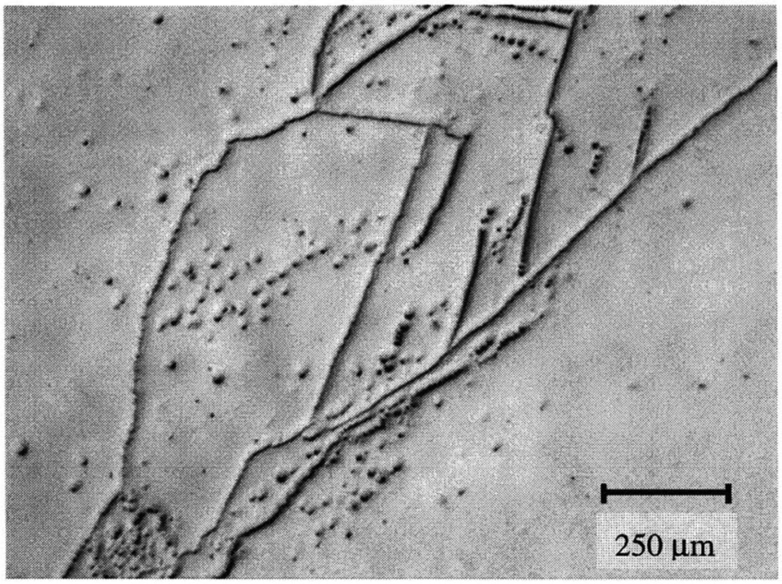

Figure 15. Low-angle grain boundaries in boule #1.

5.2.2 Boule #2

The dopant concentration for this experiment was increased slightly in order to aid in the detection of striations. Starting concentrations were chosen in order to obtain an initial dopant concentration in the crystal of $5x10^{18}$ Ga atoms/cm^3. In addition, a faster pulling rate was selected for this test in order to induce constitutional supercooling and related interface instability. The steady-state growth rate for this crystal was 13.3 mm/hr with a seed rotation of 20 rpm. The dimensions of the steady-state region were 24 mm long and varied between 18 and 21 mm in diameter. The entire boule measured 52 mm in length (fig 16).

5.2.2.1 Crystallinity

Similar to what was observed in the first crystal, four external facets were visible along the entire length of the crystal. Despite the accelerated growth rate, the solid-liquid

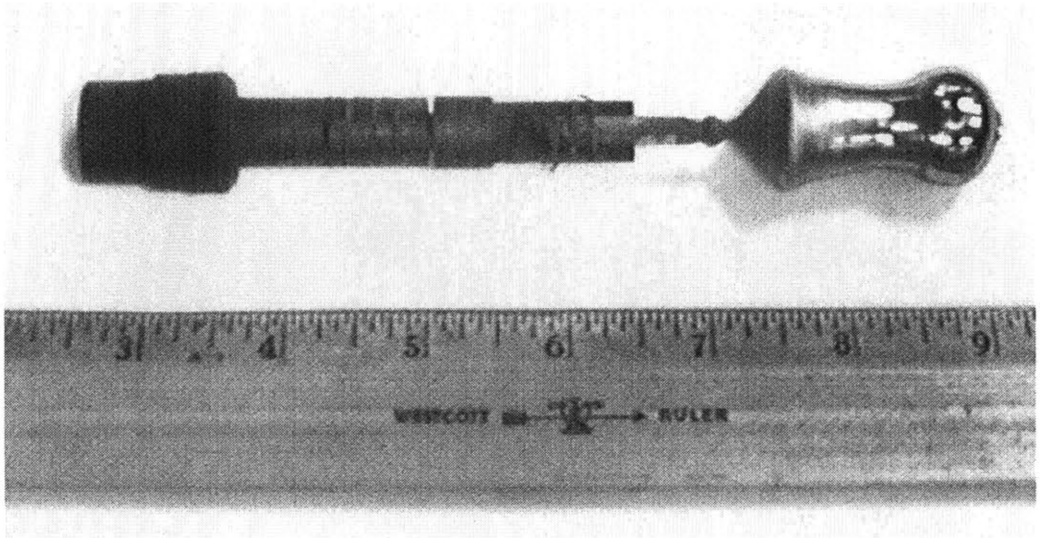

Figure 16. Boule #2 (Ga-doped Ge).

interface maintained coherency and the external crystal features indicated interface breakdown only late in the growth process. Etching revealed no evidence of interface breakdown in the interior of the boule; the entire boule was a single crystal with no detectable twin or low-angle grain boundaries.

5.2.2.2 Distribution of Solute

After etching, the axial segment revealed rotational striations by interference contrast microscopy. The striations in the steady-state growth region had a spacing of 11.2 μm with a standard deviation of 1.0 μm (fig 17), which corresponds precisely to the theoretical value of 11.1 μm/striation.

5.2.2.3 Dislocation Density

After etching, the transverse disks of this boule (both at the seed end and the bottom) appeared to be defect free using etch pits as a criterion.

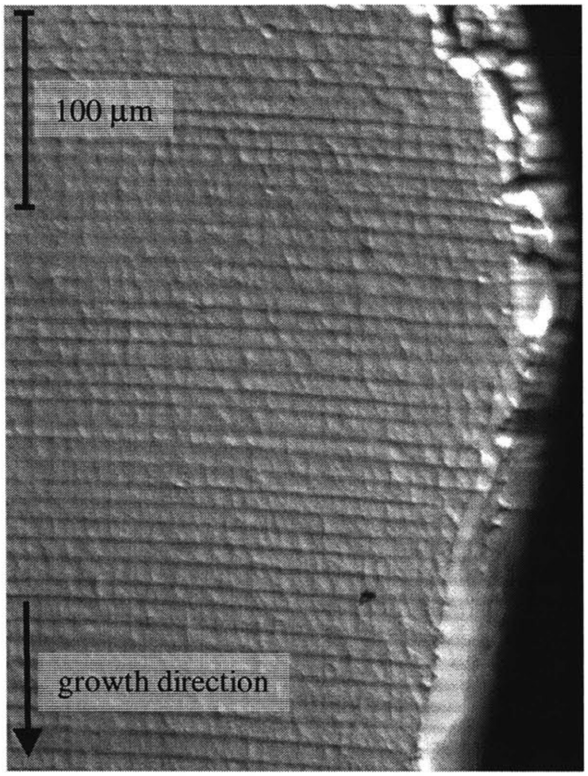

Figure 17. Rotational striations in Ga-doped Ge boule #2.

5.3 SiGe Alloys

5.3.1 Boule #3

A small amount of Si was used in this test for two reasons. First, increasing the amount of Si in the melt would increase the melting temperature significantly and complicate the seeding process when a pure Ge crystal is used. Also, it was desired to grow a single crystal, and the literature indicated that high concentrations of Si prohibit single crystalline growth.

The original attempt at growing a SiGe crystal was carried out with 0.25 at% Si in the melt. Upon melting the charge material, a thick crust developed on top of the melt. A crystal could not be seeded through this hard top layer. It was determined via Auger spectroscopy that a thin layer of silicon carbide and below that a deeper layer of silicon oxide had formed on the top of the melt. Therefore, to eliminate this crust from forming, a quartz crucible was used to grow the SiGe crystals detailed below.

The first viable SiGe growth experiment involved 0.24 at% Si, chosen to yield a concentration maximum of approximately 1 at% Si in the grown boule assuming $k_{eff} \sim 4$ for dilute Si in Ge. The average steady-state growth rate for this crystal was 5.5 mm/hr with seed rotation rate of 15 rpm. "Steady-state" growth in the <100> direction yielding a constant crystal diameter could not be achieved; rather, the diameter in this region varied between 14 and 24 mm. Hence, the steady-state growth rate cited above is an average value since the actual growth rate accelerates to 9.1 mm/hr at the maximum boule diameter (the crystal-melt interface lowers more quickly) and the actual growth rate decelerates at the minimum boule diameter to 3.7 mm/hr (the crystal-melt interface lowers more slowly). The entire boule measured 35 mm in length. After 3 mm of growth during the seeding process, the next 29 mm of the boule were grown at an average of 5.5 mm/hr, and the final 3 mm of the boule were grown at 12 mm/hr. The crystal had a maximum diameter of 24 mm (fig 18).

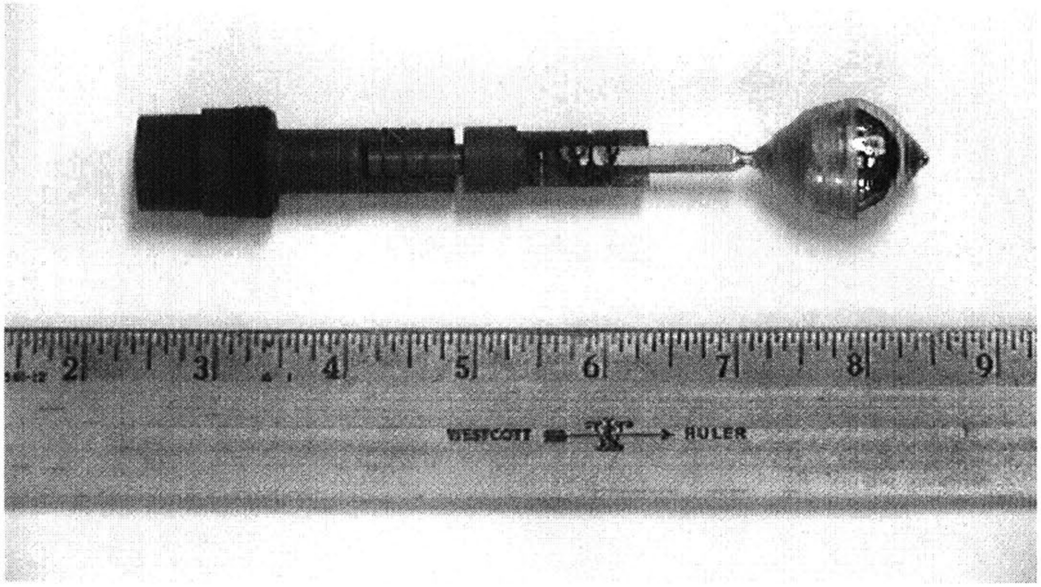

Figure 18. Boule #3 (SiGe alloy).

In order to better characterize this crystal, additional cuts were made to the boule that were not made in the Ga-doped Ge standards; the boule was cut into five sections that were individually analyzed, and the references below will follow the nomenclature given in figure 19.

5.3.1.1 Crystallinity

Four external facets on the crystal suggested single crystal growth. Also visible on the external surface, however, were several lines running axially from the initial seed-melt interface to the final portion of growth. As in the previous two crystals, the surface of the boule was smooth except for the last few mm of growth where the surface became very rough.

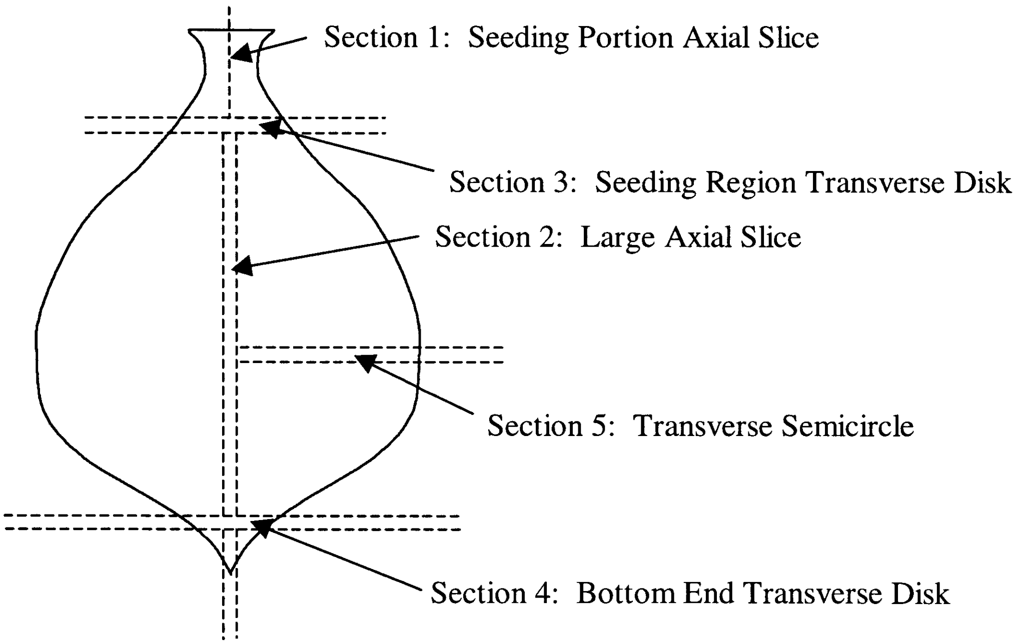

Figure 19. Schematic of cuts and sample sections for boule #3.

The seeding portion of the crystal (section 1) was mounted in plastic and cut parallel to the growth axis through the center of the boule. Microscopy revealed two grain boundaries existed in the seed that continued to propagate into the growing boule; the grain boundaries eventually merged and propagated to the free surface of the crystal.

After etching, the axial slices (sections 1 and 2) showed low-angle grain boundaries and twin boundaries propagating along the crystal axis. However, after examining the lower portions of the large axial slice (section 2) as well as the bottom end disk cut perpendicular to the growth direction (section 4), there was no indication of interface instability in the latter portions of the growth process.

5.3.1.2 Distribution of Solute

In section 2, the striations related to rotation at 15 rpm have an average separation of 6.3 μm/striation, which corresponds to that expected from the seed displacement and melt level change.

The seeding region (section 1) was also etched for striations. Most noticeable is the highly irregular interface morphology between the seed and the melt during initial growth (fig 20). The interface is faceted, with the angular deviation from normal (53.5°) suggesting the appearance of (111) facets (54.7°). The irregularities of striations at the beginning of the growing boule (directly downstream of the faceted seed-boule interface) reflect the irregularities of the original growth interface.

Approximately 1 cm into the growth process, while the boule was still shouldering, regions of the crystal had "wavy" striations indicative of an unstable interface (fig 21). The "wavy" striations suggest the onset of interface instability or as yet unexplained boundary layer effects.

Another interesting feature was detected in the striations of this boule. Near one edge of the boule, in the middle of the growth period only, the individual striations became discontinuous (fig 22). The striations appeared to have thick and thin regions, with neighboring striations directly upstream and downstream both having opposite patterns. The result was a checkerboard pattern of striations. These peculiar striations gradually took on a conventional (continuous) appearance as they proceeded toward the middle of the boule and then the striations disappeared in the central regions of the crystal. The striations on the other side of the boule did not exhibit this checkerboard pattern. This effect is as yet unexplained; it may be related to local composition changes, or it may be an etching artifact.

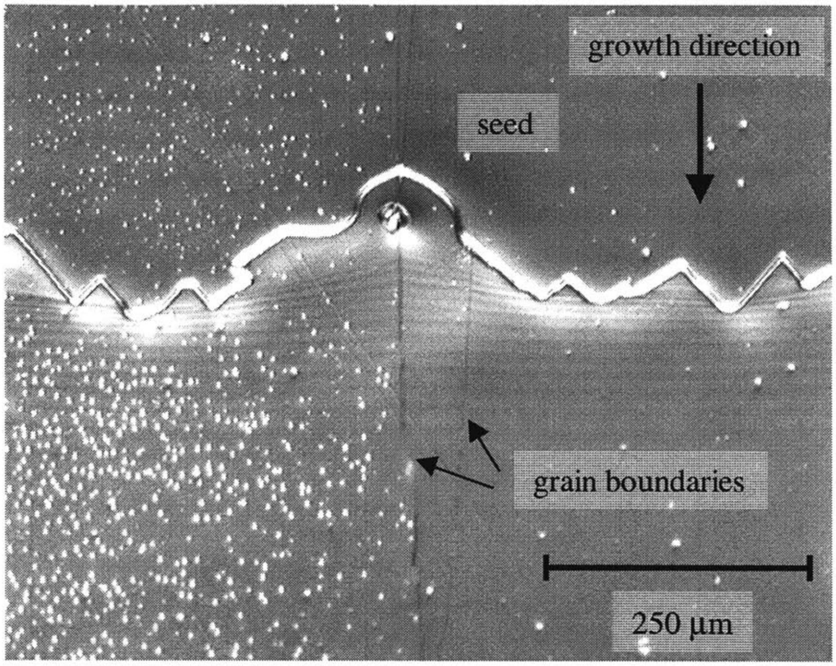

Figure 20. Interface between the seed and the initial boule growth in SiGe boule #3. Note the high dislocation density left of the grain boundaries and low dislocation density on the right side of the photograph.

Because of the peculiarity of the striation pattern (fig 22), an additional slice of the boule was cut perpendicular to the growth direction at the axial distance in which the discontinuous striations were observed (section 5). This slice was cut from the boule 17 mm below the seed-crystal interface. After etching section 5, it was discovered that the low-angle grain boundaries and a great majority of the dislocations had accumulated on the same side of the crystal in which the discontinuous striations were observed in section 2. Section 5 also exhibited a "core" (location of the center of rotation) from which solute trails spiraled out radially (fig 23). The center of the rotation core in this slice was displaced 3.8 mm from the geographic center of the crystal, indicating that the crystallographic growth direction <100> made an angle of 13° with the center of rotation.

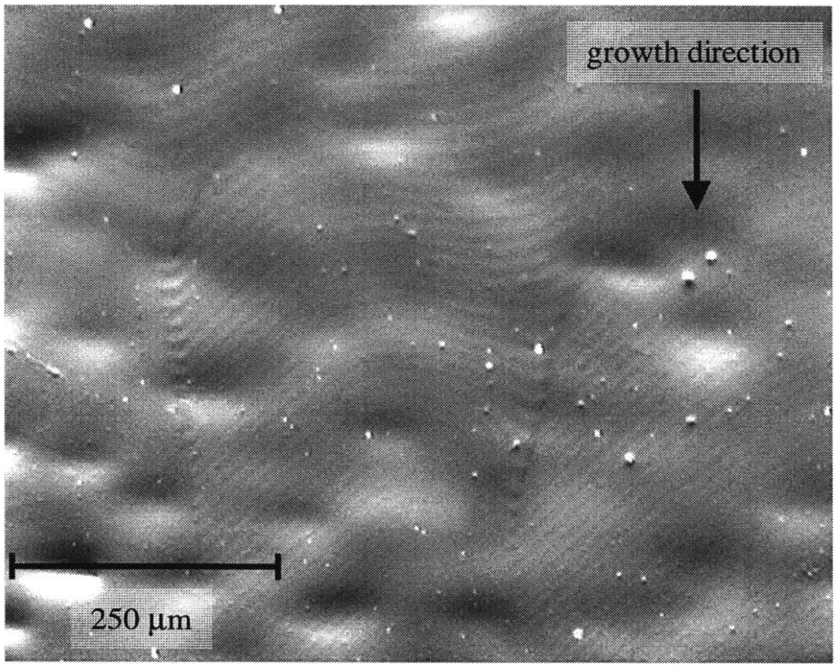

Figure 21. Wavy striations due to interface instability.

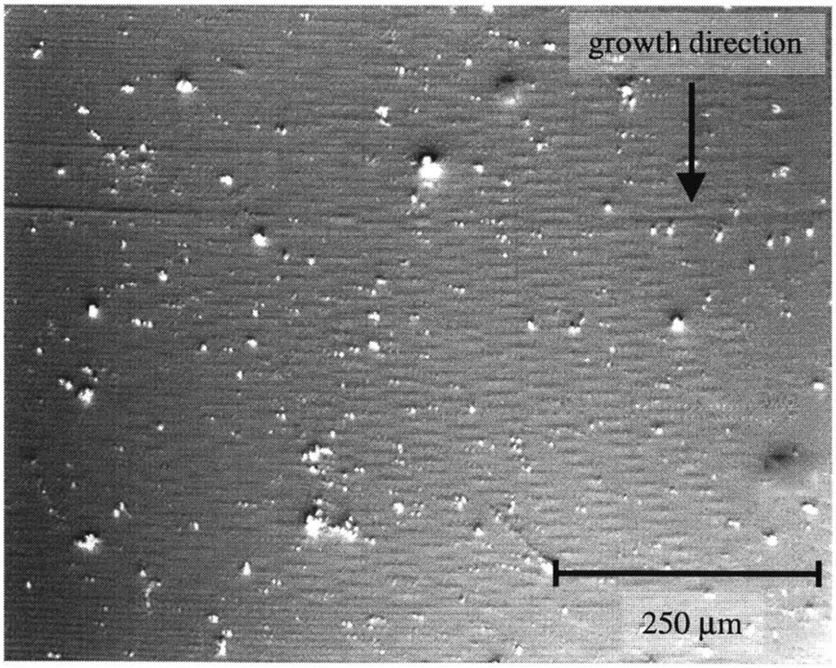

Figure 22. Checkerboard pattern found in discontinuous striations.

WDS was performed in this core pattern in order to determine the concentration of Si in the preferentially etched regions. However, the WDS device did not yield enough contrast in the surface topography to determine the sampling position in relation to the spirals of the core region. Therefore, several measurements of the Si concentration were taken at random locations in the core region. All points yielded concentrations of about 0.1 at% Si.

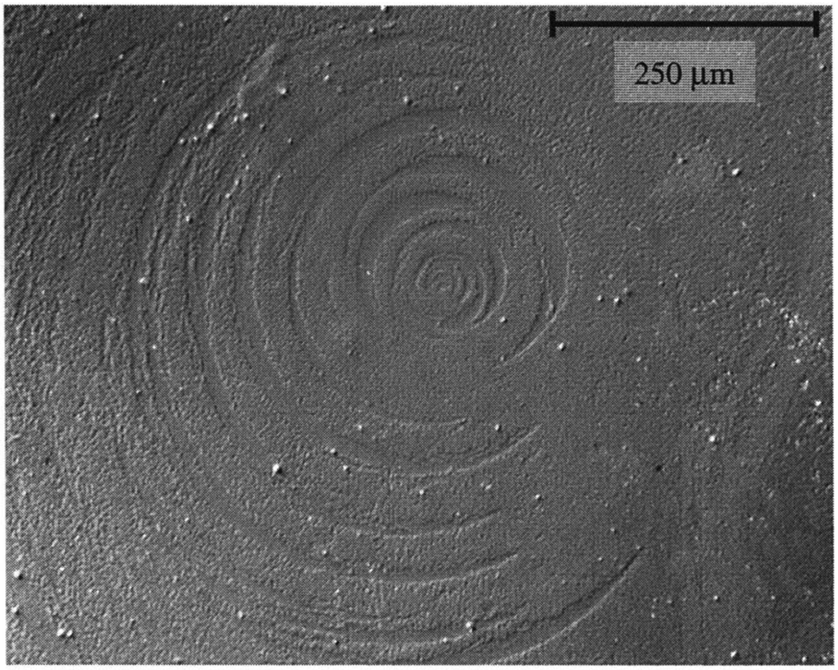

Figure 23. Core of solute about the center of rotation in SiGe boule #3.

Using WDS, the axial distribution of Si in the boule was determined. It must be noted that the axial slice for boule #3 was not etched before WDS analysis and is therefore subject to additional error due to surface contamination. The transverse slices of boule #3 and all other SiGe crystals were etched before WDS data acquisition. The maximum Si content detected in the grown boule was 0.57 ± 0.04 at% Si. Measurements taken at 10 μm spacing directly downstream of the seed-crystal interface indicated that the ramp up period of Si in the growing boule was negligible; rather, the boule attained its maximum Si concentration immediately after the beginning of growth. This fact indicates that there is no initial build-up of a solute boundary layer. Instead, the thickness of δ is negligible and it is concluded that convective currents are dominating the incorporation of solute into the crystal. In this situation, $k_{eff} = k_o$. The distribution of Si in the crystal as a function of melt volume solidified is presented in figure 24.

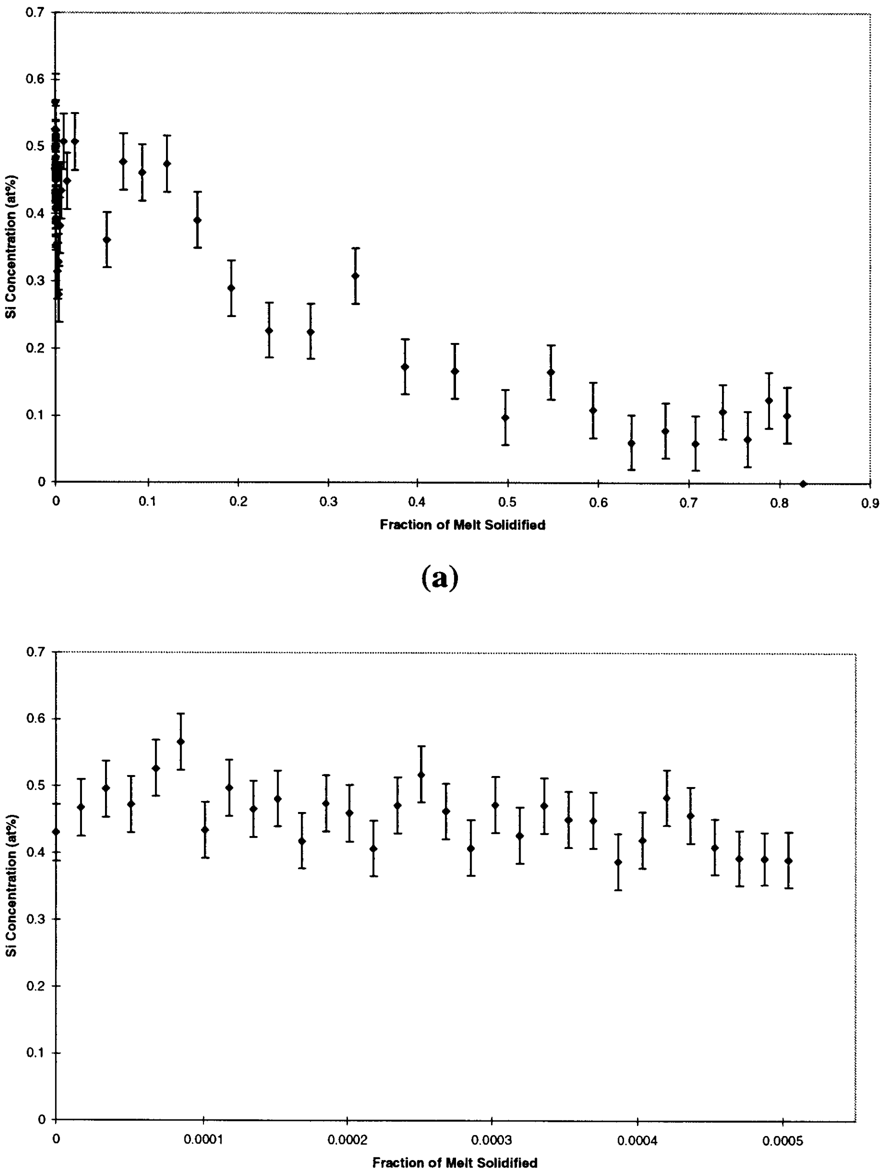

(a)

(b)

Figure 24. Distribution of silicon as a function of melt volume solidified in growth; (a) entire crystal; (b) blown up view of seeding region

k_{eff} can be determined by fitting Scheil's Equation (Eq. 1) to the experimental data (fig 17). Or, manipulating Scheil's Equation, it can be shown that:

$$\ln(C_s) = (k_{eff} - 1)\cdot \ln(1-g) + \ln(k_{eff}\cdot C_m) \qquad \text{Equation 7}$$

Plotting ln(C_s) versus ln(1-g) yields the value for k_{eff}. For this test, k_{eff} was calculated to be 2.5. As detailed in section 3.2.3, there is a wide variance of values reported in the literature for k_{eff} for dilute Si in Ge. The values for the effective segregation coefficient have been found to range from 1.8 to 6.4 for melts of just a few percent Si. The value $k_{eff} = 2.5$ found in this experiment is smaller than most values previously reported for similar Si concentrations. As expected, the macroscopic WDS concentration profile in figure 24 (a) is characteristic of convective mass transport. Pure diffusive transport would lead to a constant concentration of solute for a large portion of the boule's growth.

The Si concentration was also measured by WDS for a short distance into the seed in order to detect if any Si had diffused into the seed material during the initial growth process. The results indicate a negligible amount of Si back-diffused into the Ge seed.

X-ray diffraction was performed on boule #3 in order to determine the lattice constant of the material; this information could then be used to further confirm the Si content in the boule. The seeding axial slice was oriented by back reflection Laue to diffract from the (440) plane. The diffraction was conducted just downstream of the initial seed-melt interface (location unknown in regard to rotational striations). The d-spacing for this plane was found to be 0.9991 ± 0.0001 Å, corresponding to a lattice constant of 5.6518 Å for the material. Assuming Vegard's law is true, the expected Si concentration in the boule is 2.7 at% Si. Obviously, this value for the Si concentration is significantly higher than the results obtained by WDS, and 2.7 at% Si seems artificially high given the expected segregation coefficient. One possibility is that there is another source of lattice tensile stress in the boule that is causing the increase in the lattice constant. For example, the results of the X-ray diffraction could be high if the sample were taken within the stress field produced by a dislocation or residual surface preparation effects. But, it is possible that this lattice constant reflects a measurement of the Si concentration within a rotational striation as described in section 5.1.1.2.2 of this text.

WDS indicated only slight perturbations in the radial Si concentration for a given distance downstream in the growth process. As seen in figure 25, the Si concentration follows an oscillating pattern as one proceeds from the middle to the periphery of the boule. However, the magnitude of the relative Si concentrations cannot be precisely determined with this technique, as it can be seen that the regions of maximum Si have concentrations within the standard deviation of the regions of minimum Si. The oscillating pattern seen in figure 25 is expected, since a line drawn perpendicular to the growth axis would pass through several rotational striations.

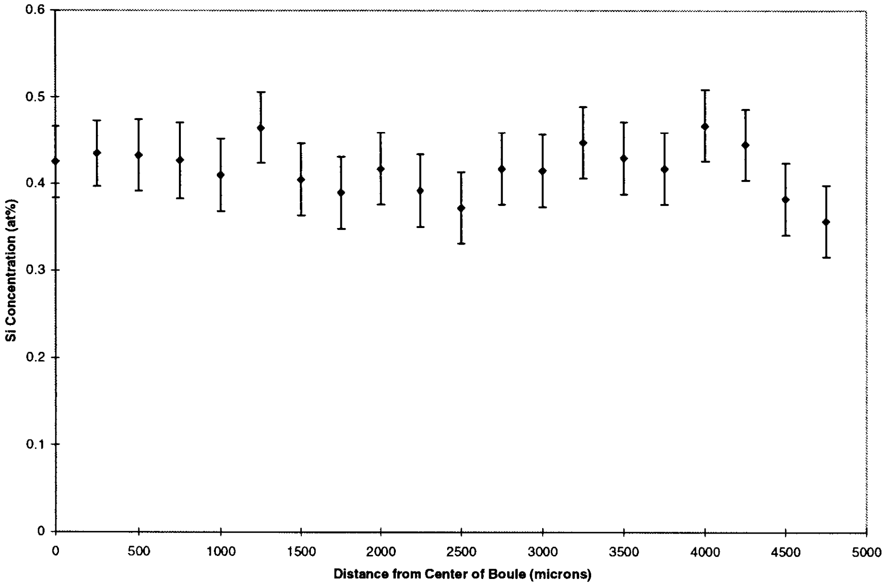

Figure 25. Radial distribution of Si in boule #3.

5.3.1.3 Dislocation Density

After etching, the seeding region disk perpendicular to the growth axis (section 3) indicated a large degree of polygonization and a high density of dislocations throughout nearly the entire cross-section of the boule. There were a few regions (approximately 25% of the surface area) in which the dislocation density was very low, presumably due to favorable orientation of the lattice structure within these regions separated by low-angle grain boundaries. Conversely, the bottom end disk (section 4) showed no indication of dislocations. This can be attributed to the fact that Si has a high segregation coefficient in Ge; this downstream region of the boule is expected to be nearly pure Ge, and therefore there is negligible lattice mismatch/strain introduced by Si in the boule. This is in contrast to the early regions of growth in which the Si is incorporated into the boule in relatively high concentrations, leading to the polygonization detected in the seeding region disk.

The seeding region of growth (section 1) also had regions of high dislocation density accompanied by regions that were effectively dislocation-free. As mentioned earlier, there existed a grain boundary in the seed that propagated into the growing crystal. On one side of this grain boundary a high (~$10^5/cm^2$) density of dislocations existed. However, on the other side of the grain boundary, the crystal grew relatively dislocation-free (see fig 20).

5.3.2 Boule #4

The goal of this growth process was to confirm the features observed in the first SiGe boule and to look for effects of varying the seed rotation rate. This experiment began with a melt composition of 0.31 at% Si. The average steady-state growth rate for this crystal was 3.8 mm/hr with a seed rotation rate of 15 rpm for a majority of the growth process. The entire boule measured 34 mm in length; the first 29 mm of the boule were grown at the steady-state growth rate and the remaining 5 mm of the boule were grown at 51 mm/hr. The steady-state region of growth had a diameter ranging from 14 to 17 mm (fig 26). In all previous growth processes the entire melt was solidified into the boule; however, in this test, only 52% of the melt was solidified.

5.3.2.1 Crystallinity

This boule was seeded at a very slow growth rate (the steady-state growth rate of 3.8 mm/hr) in order to avoid variation in the growth velocity from becoming a factor in determining the effective segregation coefficient of Si in the boule. However, at this very slow growth rate, it is difficult to initiate growth in Czochralski growth because of the relatively long time delay between external manipulation of the heat pipe temperature and its observable effect on the growing crystal's solidification rate. As a result, this crystal

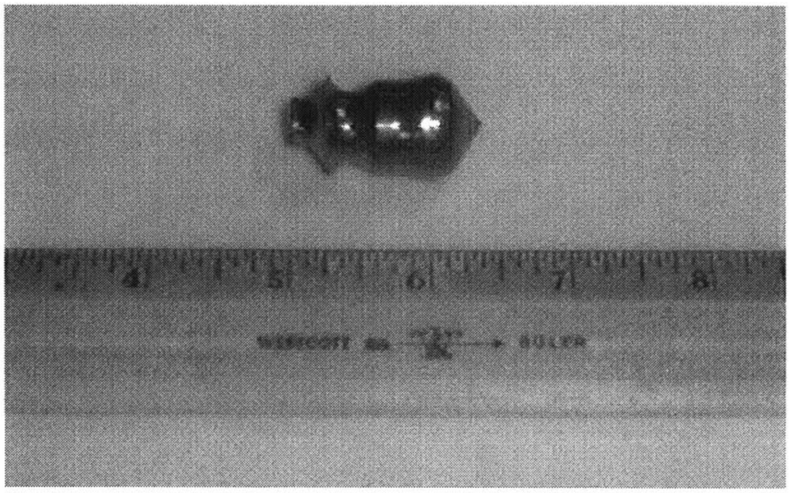

Figure 26. Boule #4 (SiGe alloy).

was cold-seeded. While cooling down after completion of the growth process, the boule broke from the seed while it was still in the pulling chamber.

Examination of the external surface of the boule indicated numerous grain boundaries running the length of the boule. In addition, only one facet was seen on the external surface of this crystal, as opposed to the four facets seen in all previous crystals. These results are expected given the cold seeding conditions. In cold seeding, some of the melt material is initially solidified on the seed at a greatly accelerated rate, causing a polycrystalline layer to grow on the bottom of the seed. Thus, the layer of polycrystalline material dictates all subsequent growth; the single crystalline nature of the seed is lost and does not continue into the growing boule.

The slices cut from the boule confirmed the polycrystallinity of the material. The axial slice revealed seven grains in the middle of the boule with boundaries oriented nearly parallel to the growth direction. The seeding region disk cut perpendicular to the growth direction indicated nine grains in this region approximately 3 mm downstream of the seed interface. The average cross-sectional area of the grains was 5 mm^2.

The last 6 mm of the crystal were grown at an accelerated rate (51 mm/hr). Even at this high growth rate, though, the interface maintained good coherency and no grains were formed during the conclusion of the growth process. Once again, as in the previous SiGe alloy, this portion of the boule is expected to be nearly free of Si due to silicon's high segregation coefficient. WDS confirmed that the Si concentration in this portion of the boule was below the minimum detection limit of 0.0177 at% Si.

5.3.2.2 Distribution of Solute

Preferential etching also revealed poor interfacial structure in a majority of the boule. Immediately after seeding, the growth striations became wavy with discontinuities in their slopes at grain boundaries and solute trails (fig 27). The solute trails faded after approximately 1 cm of growth. As seen in figure 27, the interface extended deeper into the melt material at the solute trails. This interfacial structure gives an indication of increased Si concentration in the solute trails and accelerated freezing taking place at these locations. WDS was performed across one of the solute trails. There was no quantifiable difference in Si concentration between the material inside the solute trail versus the material to either side of it.

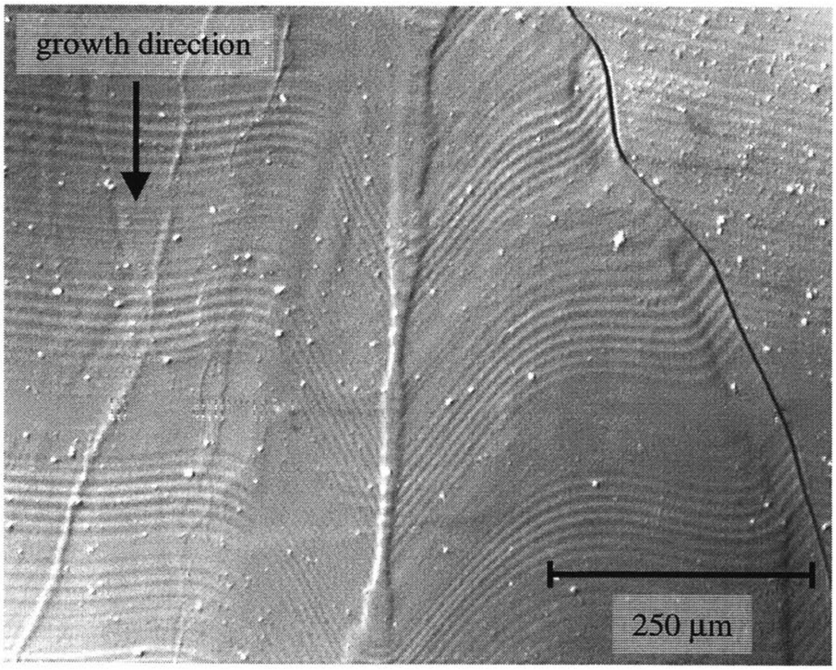

Figure 27. Solute trail and associated distortion of solid-liquid interface.

The maximum concentration of Si in the boule was 0.58 ± 0.04 at% Si (fig 28). k_{eff} for this boule was undetermined. Examining the Si content in the boule in the first stages of growth, it appears that $k_{eff} \approx 1.75$. However, when a fit of the Scheil Equation is compared to the actual Si content in the boule, the WDS data revealed much less Si in the boule as a whole than should be expected (fig 29). Given the results found in boule #6 detailed below in this work, it is possible that the polycrystalline nature of boule #4 results in the deficiency in Si along the center axis seen in figure 29. There are several other grains in the boule running coaxially to the center grain with only slightly different orientations. These grains closer to the periphery of the boule may have been preferentially oriented to incorporate more Si than the center grain in which WDS data was collected.

Examination of the radial WDS data further supports the above hypothesis of why so little Si appeared in the axial WDS data. As seen in figure 30, the Si concentration can be seen to increase nearer the free surface of the boule. This data passes through four grains running parallel to the growth direction, and indicates that the grains nearer the free surface appear to have incorporated more Si.

When growing this crystal, the seed rotation rate was varied between 15, 25, 35, and 45 rpm at two different times during the growth process. By manipulating the seed rotation rate, the forced convection is being altered and the solute boundary layer δ is changing. From the Burton, Prim, and Slichter analysis, with an increased seed rotation rate and its resulting decrease in δ, one should expect a rise in k_{eff} and therefore more solute in the boule for the regions of accelerated seed rotation (see section 3.2.3). Using the relation δ goes as (seed rpm)$^{-1/2}$, one should expect the Si content in the 45 rpm area to be 1.7x the Si concentration in the 15 seed rpm area. However, when examining the areas of seed manipulation via WDS, there was no significant change in Si concentration in the boule for the four different seed rpm rates. Therefore, this further supports the conclusion that these growth experiments were convection-controlled, and δ is very thin (there is little accumulation of solute at the solid-melt interface). As a result, as in the previous growth experiment, it is expected that $k_{eff} \cong k_o$.

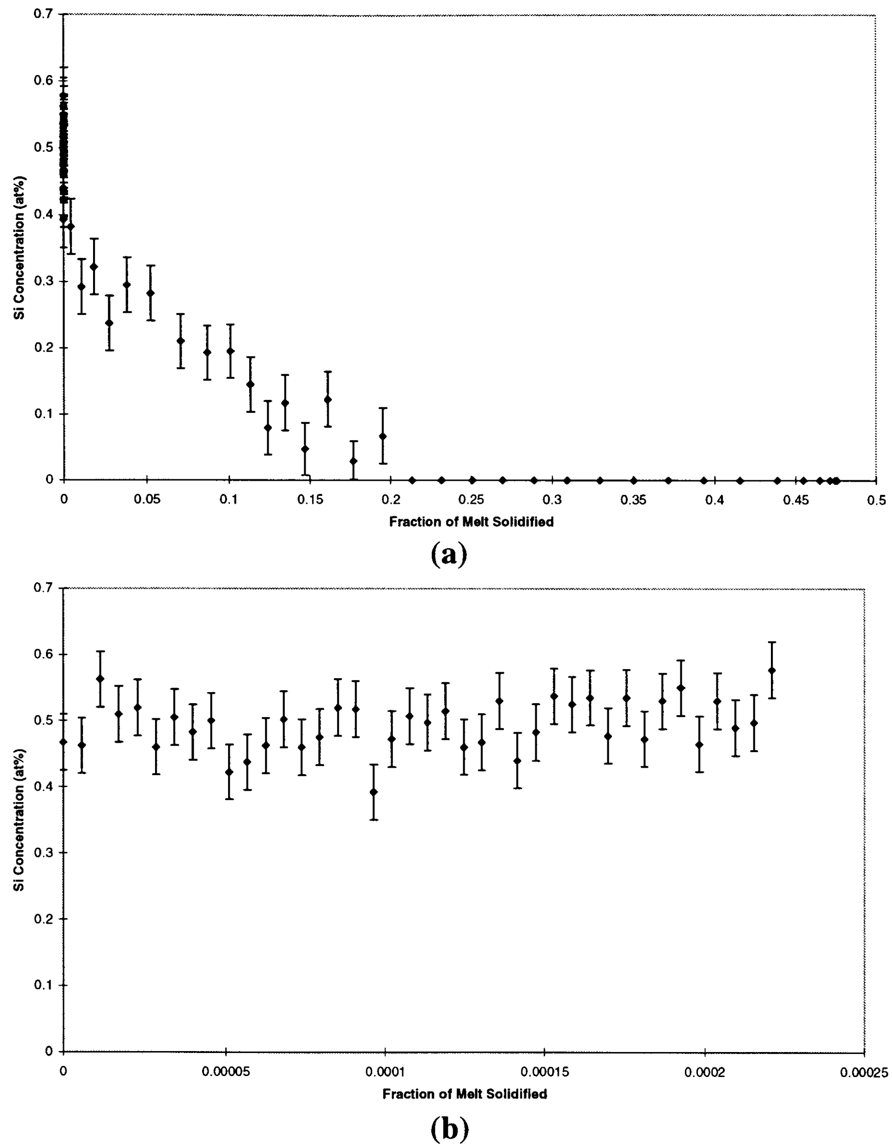

Figure 28. Distribution of silicon as a function of melt volume consumed in growth; (a) entire crystal; (b) blown up view of seeding region

For the 15 rpm portions of the crystal, we expect a striation separation of 5.5 μm. The measured striation separation was 5.7 μm with a standard deviation of 0.1 μm. For the accelerated rotation rates of 25, 35, and 45 rpm, the expected striation separation is expected to decrease to 3.3, 2,3, and 1.8 μm respectively. Given the slow growth rate for this crystal, the striation separation for the accelerated rotation rates (25, 35, and 45 rpm)

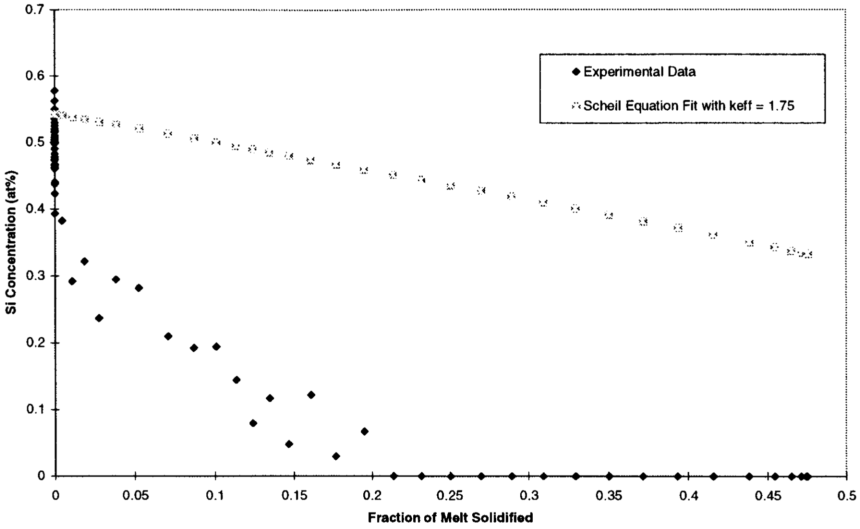

Figure 29. Fit of Scheil Equation with $k_{eff} = 1.75$.

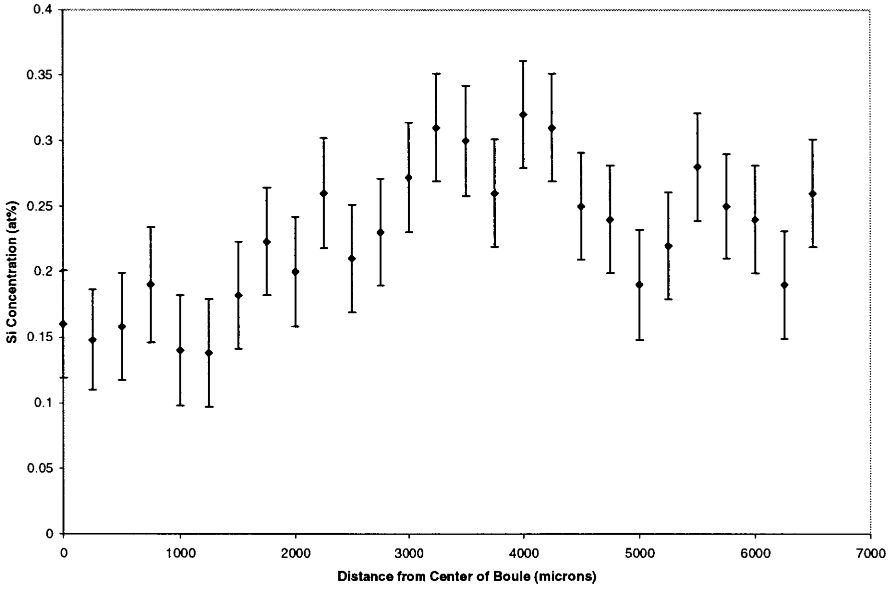

Figure 30. Radial distribution of silicon in boule #4.

was difficult to quantify because of the small separation distance. It was not possible to produce enough contrast in the striations to quantify their separation at high magnifications. For instance, at 45 rpm, given a microscopic power of 550x, the expected striation separation is only 1 mm. This magnitude of resolution/contrast could not be produced. Looking at the magnified crystal, the 25, 35, and 45 rpm striations appeared as slightly bumpy, discontinuously-banded regions in the material.

The solute trails which existed early in the growth process had disappeared by the time the two seed rotation rate manipulations occurred, so no effects of increased seed rotation on existing solute trails could be determined. The increase in the crystal rotation did not give rise to any new solute trails.

The only microscopically visible effect that occurred during accelerated seed rotation rates was the initiation of twinning in the crystal. As seen in figure 31, one grain boundary split into two to form a new grain in the material when the seed rotation rate was accelerated from 15 to 25 rpm. This new material shows bands of twins in the new grain. The material then ceased to form twins when the seed rotation rate was returned from 45 rpm back to 15 rpm.

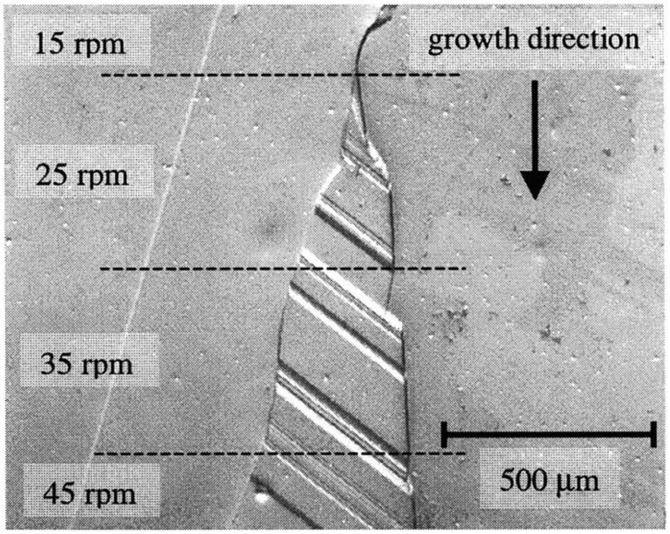

Figure 31. Initiation of twinning upon an increase in the seed rotation rate.

5.3.2.3 Dislocation Density

The seeding region transverse disk, cut 6 mm downstream in the boule, was etched for dislocations. There were no detectable dislocation pits in the material. However, as mentioned earlier, this section of material had several grain boundaries. From the WDS analysis, it was seen that the Si concentration in this region is 0.25 at% Si. From the other boules grown, it was found that this amount of Si in the boule was more than enough to cause lattice mismatch resulting in dislocation formation. However, in this boule, the polycrystalline nature of the alloy seems to have accommodated the lattice mismatch in order to prevent any dislocations from forming within the relatively small grains.

5.3.3 Boule #5

The melt in this growth experiment was composed of 0.23 at% Si. A steady-state diameter was never achieved during growth. The steady-state pull rate was 2.79 mm/hr. This pull rate was initiated when the crystal diameter was 23 mm and growing. After reaching a maximum diameter of 29 mm, the boule began to neck down to a smaller diameter (due to an increase in the melt temperature), but soon all of the melt material had been incorporated into the crystal. The length of the boule grown at the steady-state pull rate was 15 mm. At the minimum boule diameter (23 mm), the growth rate was 7.5 mm/hr. Near the end of the boule at the maximum diameter (29 mm), the growth rate was 11.0 mm/hr. The total length of the crystal was 35 mm plus the small extension (4 mm) at the end of the crystal in which the final melt material solidified (fig 32). The boule diameter can be seen to decrease rapidly in the final few mm of growth as the melt material was exhausted.

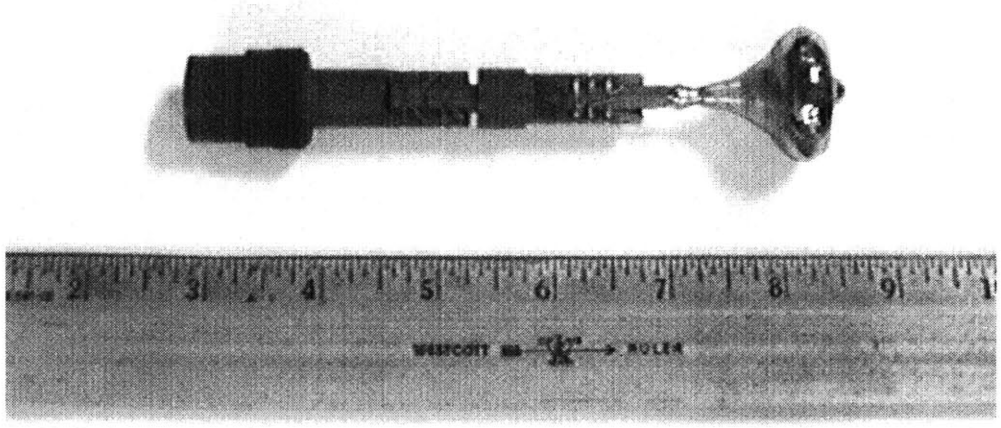

Figure 32. Boule #5 (SiGe alloy).

5.3.3.1 Crystallinity

The external surface of the boule exhibited four facets indicative of single crystalline growth. However, examination of the surface also indicated that there were several twin boundaries running along the surface of the boule for the entire growth process.

The axial slice showed no indication of grain boundaries after etching. The only grain boundary found in the material was at the very end of growth. The grain boundary was oriented perpendicular to the growth direction and separated the wide portion of the boule from the small extension (last 4 mm) at the end of growth in which the melt material was expired.

Two disks were cut from the boule perpendicular to the growth direction. The seeding region disk was cut 13.5 mm downstream of the initial seed-melt interface, and the bottom end disk was cut 5 mm above the end of the boule. After etching both of the disks, no grain boundaries were evident in the boule.

5.3.3.2 Distribution of Solute

After preferentially etching the seeding region, the seed-boule interface became apparent. Unlike the first SiGe boule grown in which the interface took on a jagged appearance due to faceting along {111} planes, the interface for this crystal was more planar. It was observed that the seed melted much deeper on one side, and then the seed-melt interface swept across the boule perpendicular to the growth direction with no faceting (fig 33). All of the solute boundary trails existed on the side of the boule in which much more of the seed material had melted. The solute boundary trails existed for only the first 5 mm of growth; the rest of the crystal showed no indication of interface breakdown. The incoherency of the interface at the solute trails can be seen in figure 34, in which the striations are continuous on either side of the solute boundary trail but non-existent within it.

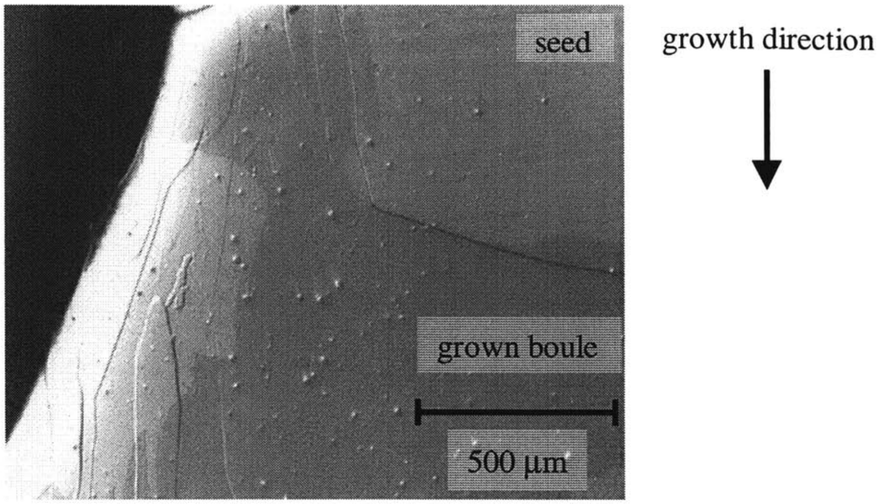

Figure 33. Seed-crystal interface of boule #3.

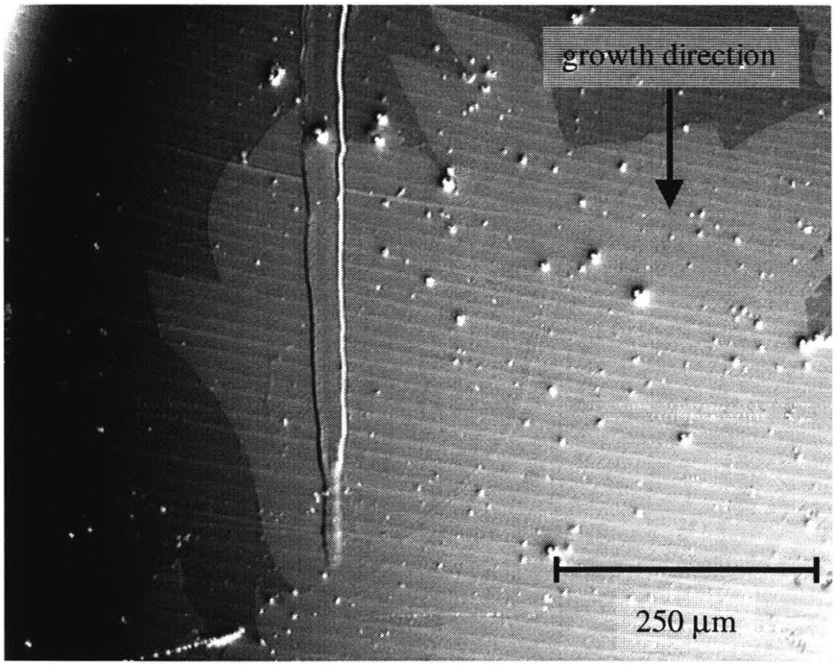

Figure 34. Disappearance of rotational striations within a solute trail.

The external surface of the boule at the end of the growth process exhibited a spiral pattern radiating out from the center of the boule. This pattern could have been a result of how the boule rubbed against the crucible at the conclusion of growth. But, it was also thought that the pattern could have been a result of uneven radial dopant distribution in the crystal. After preferentially etching the transverse disk near the end of growth, there was no indication of any spiral pattern of preferential etching; this confirms that the exterior surface pattern was a result simply of how the last portions of the melt solidified while scraping against the crucible. The preferential etching of the transverse disk did show a circular striation pattern, though. The striations were well centered about the geographic center of the boule, indicating that the thermal center of the melt was well aligned with the center of the growing crystal. Near the center of the boule, the measured striation separation was 61 μm/striation. Near the edges of the boule, the striations formed closer together with a measured striation separation of 49 μm/striation. These striations could result from cyclic temperature fluctuations in the melt. As the melt temperature cycles, the interface location moves up and down due to cyclic melting and refreezing of material. The striation pattern seen in this boule is in contrast to the spiral pattern observed in boule 3, in which fluid flow effects resulted in a spiral pattern of solute seen in the transverse piece (see fig 23).

The maximum Si concentration in the boule was 0.51 at% Si (fig 35). k_{eff} for the boule was determined to be 3.0 (see fig 17). As in boule #3, the concentration of Si was measured by WDS to be effectively constant for the entire radius of the boule.

As in the previous growth process, the seed rotation rate was varied in this test between 15, 25, 35, and 45 rpm. The seed rotation rate manipulations were conducted when the boule was at its widest diameter. Therefore, for 15 rpm, the expected striation separation for the growth conditions was 12.2 μm/striation. The measured striation separation was 12.0 μm/striation with a standard deviation of 1.9 μm. For the 25 rpm region of growth, the expected striation separation was 7.3 μm/striation. The measured value was 7.5 μm/striation with a standard deviation of 0.3 μm. As in the previous boule grown, the striation separation for the 35 and 45 rpm cases was not quantifiable. Rather, the high rotation rates did not result in any definable band structure that could be quantified.

After etching for striations, another feature was detected in the striation pattern. Near the edge of the crystal on both sides, the rotational striatia bent up 34° from the internal

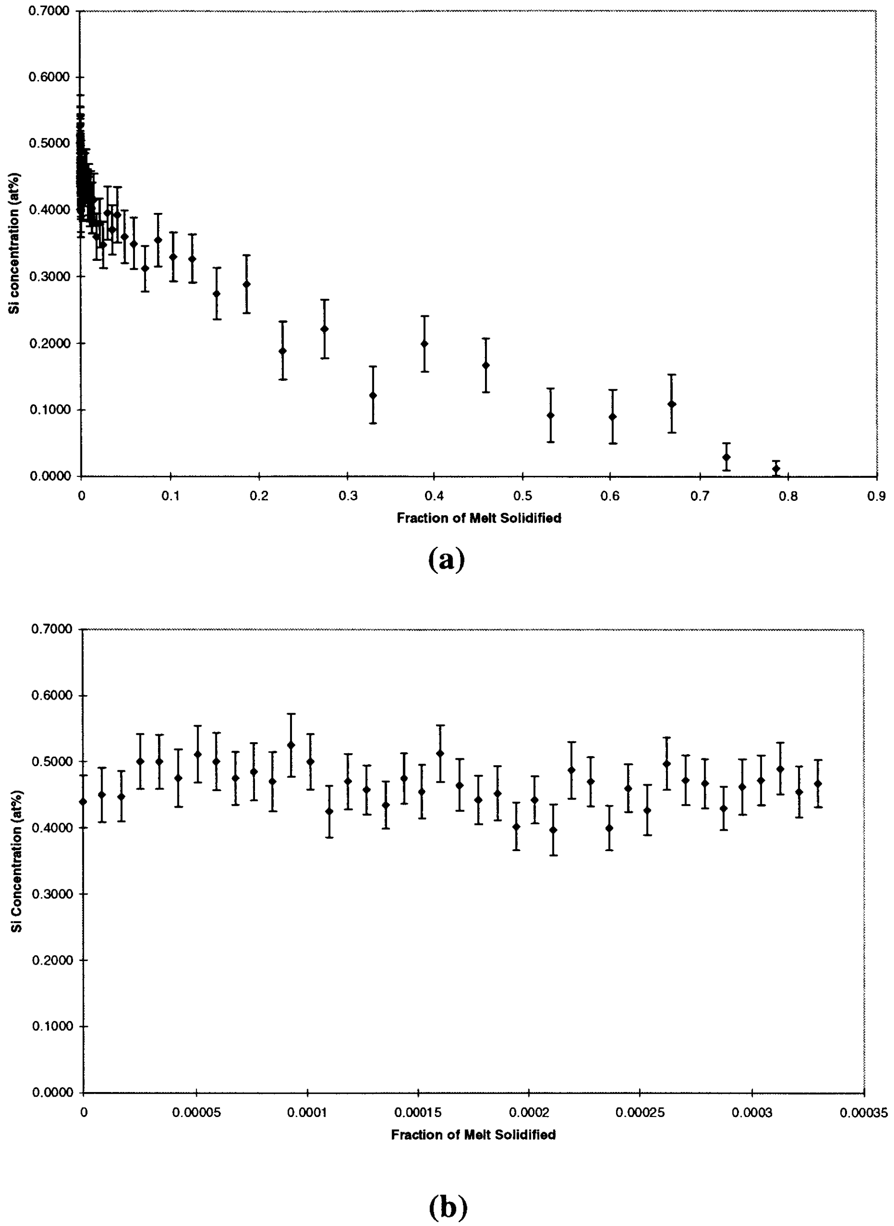

Figure 35. Distribution of silicon as a function of melt volume consumed in growth; (a) entire crystal; (b) blown up view of seeding region

striations (fig 36). However, the internal striations were not perpendicular to the growth direction at this location near the crystal periphery; rather, the internal striations were curved up 21°, resulting in the edge striations being oriented a total of 55° from the growth direction. Therefore, this striation orientation corresponds to faceting along {111} planes. The facets are visible in this axial slice because the slice was cut through two of the four facets that form on the exterior of the boule during <100> growth. The faceting of the striations extended for nearly the entire length of the boule.

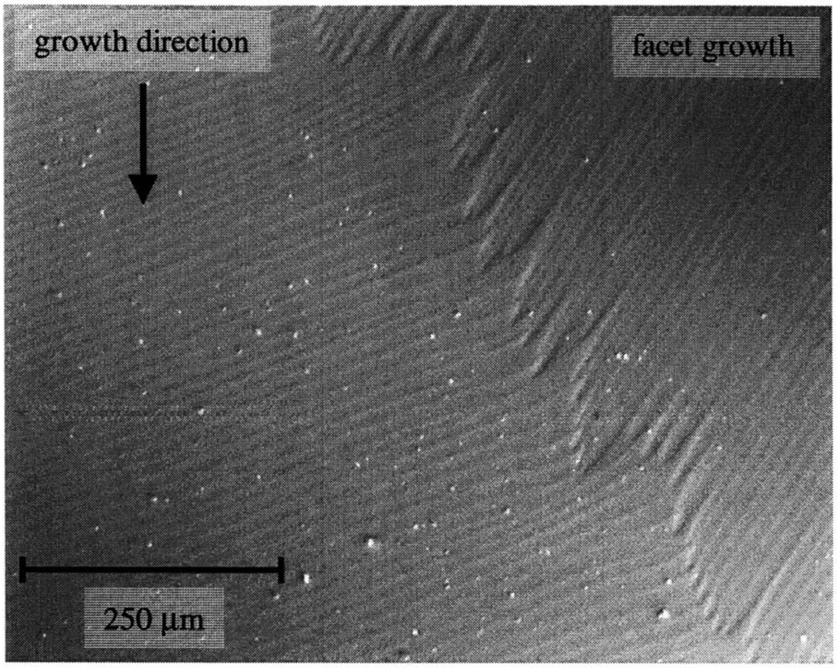

Figure 36. Faceting on {111} planes during <100> growth.

5.3.3.3 Dislocation Density

The seeding region transverse disk showed a relatively high density of dislocations on average. There were pockets of material in which the defect density was dense, and other regions appeared defect-free. The highest density of the etch pits in this disk was 10^5/cm^2. In some regions the defects could be observed to line up in order to reduce their total energy (fig 37), thereby forming low-angle grain boundaries.

The bottom end transverse disk of material cut from the boule near the end of the growth process also showed a high degree of dislocations (highest density: $5\text{x}10^4$/cm^2). As in the seeding region transverse disk, some regions appeared dislocation-free while other regions had high etch pit densities.

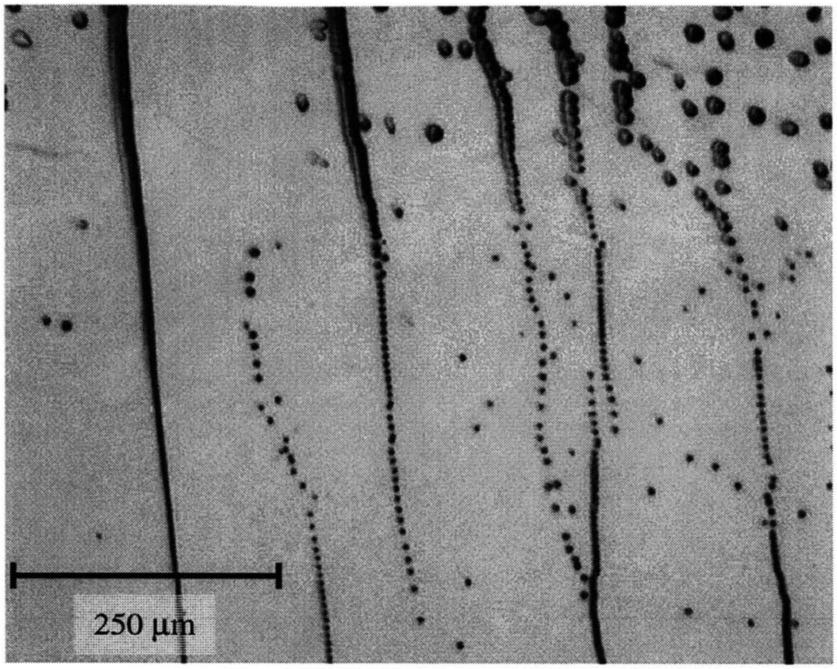

Figure 37. Dislocations lining up to reduce their energy, thereby forming low-angle grain boundaries in boule #5.

5.3.4 Boule #6

Attempts to grow with higher concentrations of Si in the melt were not successful. The material was very difficult to seed, as the seed material would begin to melt at the same time that the top of the melt material was starting to resolidify. The crucible was moved axially in the heat pipe in order to manipulate the thermal gradient at the interface, but a stable configuration (in which the solid seed could be dipped into an entirely liquid melt) was never achieved.

This boule was grown with a larger percentage of Si, but as will be detailed below, it was grown at a greatly accelerated rate and experienced complete interface breakdown. This boule was grown with 3.2 at% Si in the melt. There was no rotation of the seed during the growth process. The boule was grown at 20 mm/hr for the first 10 mm of growth and then the crystal was grown at 35 mm/hr for the final 3 mm of growth. The maximum diameter of the boule was 31 mm (the diameter was always rapidly changing), and the entire boule measured 13 mm in length (fig 38). 70% of the initial melt material was solidified into the boule.

Figure 38. Boule #6 (SiGe alloy).

5.3.4.1 Crystallinity

The entire surface of the boule was rough. Ridges indicative of dendritic growth covered the top exterior surface of the boule. When a transverse disk was cut from the boule perpendicular to the growth axis, the interior grains maintained the dendritic pattern found on the top exterior surface. Upon etching the disk for grain boundaries, the high degree of polycrystallinity that was expected became apparent. In addition, the interior of the grains took on a rippled appearance (not seen in any of the other crystals) due to the unstable interface resulting from the accelerated growth rate (fig 39).

The axial slice indicated the high degree of polycrystallinity expected. The boule had numerous (~100) individual grains in the axial cross-section.

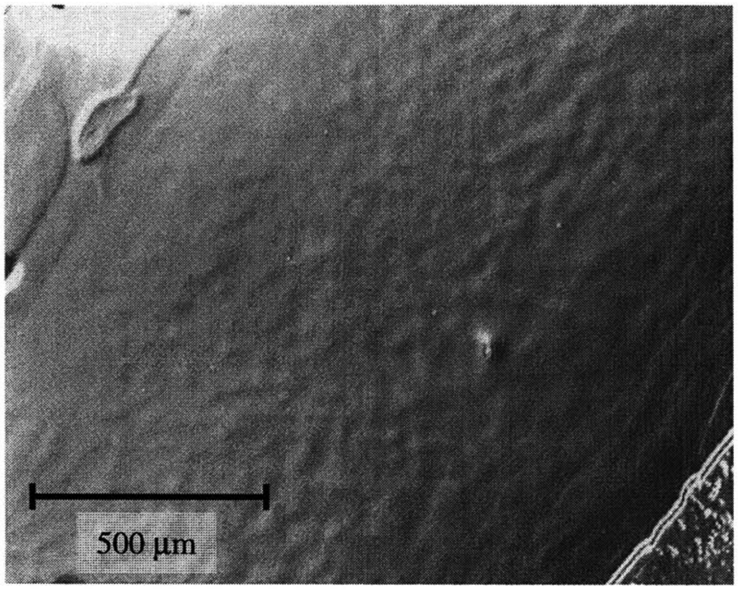

Figure 39. Rippled cross-section indicative of an unstable interface during the growth of boule #6. Growth direction into the paper.

5.3.4.2 Distribution of Solute

Because this boule was grown without any seed rotation, no rotational striations could form. Therefore, any striations in the boule would be due to temperature fluctuations in the melt at the crystal-melt interface (fundamental striations, a result of convection). After etching, however, no striations were visible in the boule.

Because the melt was superheated in comparison to the seed, the seed-crystal interface at the beginning of growth was highly irregular. Figure 40 indicates how a portion of the seed-crystal interface took on the {111} faceted structure found earlier in the first SiGe boule grown. However, as evident in the figure, there were also other regions in which the seed melted substantially. The relatively high concentration of Si in these regions is evident from the preferential etching process. Within just a couple of mm downstream of the seed-crystal interface, the boule became polycrystalline.

WDS indicated no regular pattern to the axial Si distribution. The maximum Si concentration in the boule was measured to be 3.43 at% Si. The Si concentration

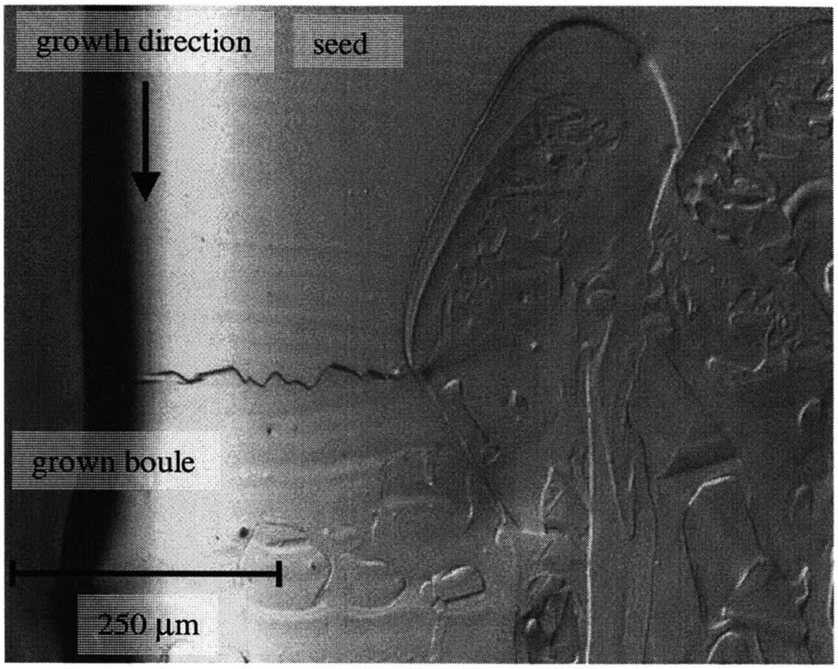

Figure 40. Seed-melt interface in boule #6.

continuously increased to this value for the first 3.5 cm of growth, but then the Si concentration oscillated greatly for the rest of the boule (fig 41). There are several possible explanations for the irregular distribution of solute shown in figure 41; all of the reasons revolve around the polycrystalline nature of the boule. First, as proposed in section 5.3.2.2 of this text, k_{eff} may be orientation-dependent, and therefore Si was incorporated into some preferably favored grains faster than other grains. Also, grain boundary segregation effects may result in the erratic segregation. In addition, at each grain in this fast growth process, the solute boundary thickness δ is continuously changing as the interface morphology changes. All of these effects have probably contributed to the erratic Si distribution exhibited by the axial data in figure 41.

Given the maximum Si concentration of 3.4 at% Si in the boule and the starting melt composition of 3.2 at% Si, it is determined that k_{eff} is only slightly greater than 1 for this growth. This is expected, as k_{eff} is expected to go to 1 as the growth velocity approaches infinity.

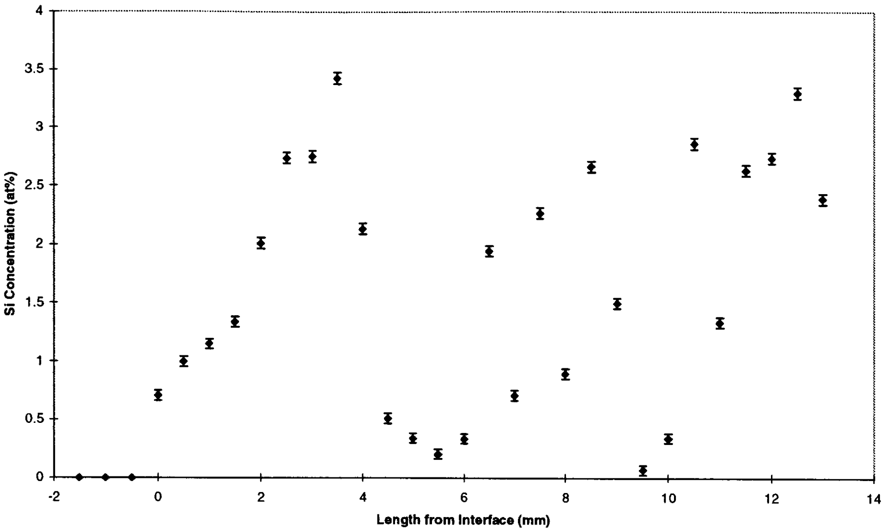

Figure 41. Axial distribution of silicon in Boule #6.

5.3.4.3 Dislocation Density

A transverse slice showed a majority of the grains had few or no dislocations in their interior. However, a few of the grains had extremely high (>10^7/cm^2) densities of dislocation etch pits. These grains of high dislocation density often neighbored an apparently dislocation-free grain.

CHAPTER 6: SUMMARY AND CONCLUSIONS

Various features of crystallinity (polycrystallization, twin boundaries, and low-angle grain boundaries leading to polygonization) were observed in this work. The concentration of Si in the melt was the primary factor controlling the crystallinity and structural perfection of the grown boule. Nonuniform Si distribution was seen to cause unstable interfaces and the formation of solute trails which resulted in the initiation of grain boundaries. In the single crystals grown, low-angle grain boundaries and twin boundaries were always observed. Polycrystalline growth was the result when there was more than 1 at% Si in the boule. No effect on the crystalline structure was observed for various growth velocities. The results indicated that, as expected, it is much easier to grow single crystals of Ga-doped Ge than dilute SiGe alloys.

The effective segregation coefficient for this work was found to be 2.75, which is slightly lower than the average value for k_{eff} quoted in the literature. It was also observed that the concentration of Si in the boule depended heavily upon the grain orientation during growth. Small changes in crystallographic orientation had a large effect on the rate of Si incorporation. No effect on the macrosegregation was observed for seed rotation rates of 15 to 45 rpm, indicating that the growth was convection driven.

Microsegregation via rotational striations was observed in all of the boules grown in this work. The rotational striations result from radial thermal asymmetry coupled with compositional differences radially in the melt, although the degree of non-uniformity was too low to measure quantitatively with the analytical techniques used herein. The rotational striations disappeared in the center of the boules, as the interface in the middle of the boules was more planar and did not experience localized meltback and accelerated growth rates with each revolution of the boule. Constitutional supercooling was seen to form solute trails in several of the boules, but a full cellular structure was never observed. Only ~ 0.5 at% Si in the crystal was needed to cause solute trails to form.

Other microsegregation effects at the crystal-melt interface were observed in this work that are not detailed in the literature. Interface instability via "wavy" striations was seen in the interior of a crystal. Also, discontinuous striations forming a "checkerboard" appearance were observed. Also, as predicted in the literature, faceting at the seed-crystal interface was observed for growth from <100> seeds.

The Ga-doped Ge boules contained far fewer dislocations than the SiGe alloys. One of the Ga-doped Ge boules contained low-angle grain boundaries and regions of 2500 dislocations/cm^2, but the other Ga-doped Ge boule appeared dislocation free. The SiGe single crystals, on the other hand, had regions of large (~10^5/cm^2) dislocation density when the Si concentration approached 1 at% in the boule. Other regions of the crystals (in other grains with less Si or downstream in the boule when virtually all of the Si had been depleted) indicated dislocation-free growth.

The goals set at the beginning of this work were not obtained in full. *(1)* A single crystal of 5 at% Si was never obtained, even though the literature reported growth conditions resulting in this type of crystal. *(2)* In the crystals grown in this work, dislocation densities less than 10^5/cm^2 were obtained, but only for very low concentrations of Si (~ 0.5 at%) in the boule. *(3)* A repeatable value for k_{eff} was found in the two single crystalline boules. However, the value of k_{eff} for this work (2.75) is lower than the average value found in the literature for similar concentrations of Si in Ge (~4).

CHAPTER 7: RECOMMENDATIONS FOR FUTURE WORK

Optical analytical techniques were attempted to better characterize the boules grown, but they were unsuccessful. UV/VIS spectroscopy was performed to determine the bandgap of the material and therefore the composition. However, because SiGe is an indirect bandgap material, it was found that the transition from reflection to transmission was too broad in wavelength to determine the Si concentration in the crystal. Next, FTIR was attempted in order to find characteristic peaks for Si and Ge and therefore determine the composition of the alloys. However, FTIR also was unsuccessful because it did not provide enough resolution in the data for the small concentrations of Si used in this work.

In future work, techniques such as measurement of the Hall effect may be used in order to determine the carrier densities when such low concentrations of Si exist in the boule and to determine the small changes in Si concentration in the solute trails. X-ray fluorescence may also be an effective method to characterize dilute SiGe alloys.

Future work should include determination of the solute distribution within and immediately surrounding rotational striations. Axial WDS data in this work never revealed significant variations in Si concentration that could be attributed to the presence of a striation. Improved measurements of the microsegregation will lead to more precise calculation of the internal stresses due to solute segregation. Also, as mentioned in section 5.1.1.2.2, X-ray diffraction measurements could be performed within and around a rotational striation to determine the internal stresses due to microsegregation.

Another interesting experiment would be to alloy Ge with both Si and Ga simultaneously. The behavior of Ga in Ge is well-known and documented. Adding Ga to the melt should aid in evaluating the formation of Si striations, especially since Ga segregates in the opposite direction (to the bottom) as opposed to Si (to the top).

Further study of the SiGe system should take place in a microgravity environment and in a centrifuge to study gravitational effects on the diffusion boundary layer δ. The Si-Ge system is strongly segregating, making it extremely sensitive to convection states (which are usually gravity driven). It is expected that gravity would have an influence on the mixing or de-mixing of a solid solution with constituents that differ considerably in density. Therefore, in a high-g environment, the macroscopic distribution profile is expected to be dependent upon the direction of solidification in respect to the g-vector. Ingots solidified in a microgravity environment should be relatively unaffected by the solidification direction. To date, though, results in this field of study have been contradictory and inconclusive.

An encapsulant may also be used in future growth experiments. An encapsulant has been found to aid in reducing segregation effects in semiconductor growth. Liquid B_2O_3 encapsulant has been found to reduce convective melt flows in Czochralski systems. The suppression of convective flow in the melt results in the disappearance of microsegregation inhomogeneities and virtually eliminates radial segregation in Ga-doped Ge (46). Also, $CaCl_2$ encapsulant has been found to prevent nucleation in Bridgman growth (8) and liquid-encapsulated zone melting (47).

BIBLIOGRAPHY

1. Rosi F.D. 1968. *Solid-State Electronics*, **11**: 833.
2. Rowe D.M. 1987. *Journal of Power Sources*, **19**: 247.
3. Kurten M., Schilz J. 1994. *Journal of Crystal Growth*, **139**: 1.
4. Dahlen A., Fattah A., Hanke G., Karthaus E. 1994. *Crystal Research Technology*, **29**: 187.
5. Wollweber J., Schulz D., Schroder W. 1995. *Journal of Crystal Growth*, **163**: 243.
6. Hansen M. 1958. *Constitution of Binary Alloys*, p. 774. New York: McGraw-Hill Book Company, Inc. 1305 pp.
7. Fitzgerald E.A. 1995. *Annual Review of Materials Science*, **25**: 417.
8. Kadokura K., Takano Y. 1997. *Journal of Crystal Growth*, **171**: 56.
9. Abrosimov N.V., Rossolenko S.N., Alex V., Gerhardt A., Schroder W. 1996. *Journal of Crystal Growth*, **166**: 657.
10. Chi J.Y., Gatos H.C. 1979. *Journal of Applied Physics*, **50**: 3433.
11. Jastrzebski L., Lagowski J., Walukiewicz W., Gatos H.C. 1980. *Journal of Applied Physics*, **51**: 2301.
12. Walukiewicz W., Lagowski J., Jastrzebski L., Rava P., Lichtensteigen M., Gatos C.H. 1980. *Journal of Applied Physics*, **51**: 2659.
13. Schilz J., Romanenko V.N. 1995. *Journal of Materials Science: Materials in Electronics*, **6**: 265.
14. Martin E.P., Witt A.F., Carruthers J.R. 1979. *Journal of the Electrochemical Society*, **126**: 284.
15. Xing Z.J., Kennedy J.K., Witt A.F. 1982. *Journal of Crystal Growth*, **59**: 659.
16. Pfann W.G. 1952. *Journal of Metals*, **4**: 747.
17. Pfann W.G. 1966. *Zone Melting*, 2nd ed, p. 11. New York: John Wiley and Sons, Inc. 310 pp.

18. Scheil, E. 1942. *Zeitschrift fur Metallkunde*, **34**: 70.

19. Burton J.A., Prim R.C., Slichter W.P. 1953. *The Journal of Chemical Physics*, **21**: 1987.

20. Helmers L., Schilz J., Bahr G., Kaysser W.A. 1995. *Journal of Crystal Growth*, **154**: 60.

21. Zhang W., Yan S, Ji Z. 1996. *Journal of Crystal Growth*, **169**: 598.

22. Wagner C. 1954. *Journal of Metals*, **6**: 154.

23. Smith V.G., Tiller W.A., Rutter J.W. 1955. *Canadian Journal of Physics*, **33**: 723.

24. Yue A.S., Yue J.T. 1972. *Journal of Crystal Growth*, **13/14**: 797.

25. Favier J. 1980. *Journal of Crystal Growth*, **49**: 373.

26. Witt A.F., Gatos H.C., Lichtensteiger M., Herman C.J. 1978. *Journal of the Elecrochemical Society*, **125**: 1832.

27. Romanenko V.N., Smirnov Y.M. 1970. *Inorganic Materials*, **6**: 1527.

28. Rouzaud A., Camel D., Favier J.J. 1985. *Journal of Crystal Growth*, **73**: 149.

29. Yonenaga I., Matsui A., Tozawa S., Sumino K., Fukuda T. 1995. *Journal of Crystal Growth*, **154**: 275.

30. Brice J.C. 1965. *The Growth of Crystals From the Melt*, pp. 80-88. New York: John Wiley and Sons, Inc. 192 pp.

31. Coriell S.R., Sekerka R.F. 1979. *Journal of Crystal Growth*, **46**: 479.

32. Coriell S.R., Boisvert R.F., Rehm R.G., Sekerka R.F. 1981. *Journal of Crystal Growth*, **54**: 167.

33. Abrosimov N.V., Rossolenko S.N., Thieme W., Gerhardt A., Schroder W. 1997. *Journal of Crystal Growth*, **174**: 182.

34. Belokurova I. N., Kekoua M.G., Petrov D. A., Suchkova A.D. 1959. *Izv. Akad. Nauk. SSSR. OTN. Metallurgija I toplivo*, **1**: 9

35. Selikson B. Aug 22, 1961. Patent No. US 2,997,410.

36. Tairov S. J., Tagirov V.J., Shakhtakhtinskii M.G., Vigdorovich V.N., Kuliev A.A. 1967. *Doklady Akad Nauk SSSR*, **176**: 851.

37. Dolivo-Dobrovol'skaya G.I., Smirnov Y.M. 1975. *Inorganic Materials*, **11**: 1001.

38. Tairov S.J., Tagirov V.J., Shakhtakhtinskii M.G., Kuliev A.A. 1966. *Sov. Phys. Crystallogr.*, **10**: 632.

39. Tagirov V.J. 1983. Edition ELM, Baku (Azerbadjan).

40. Bardsley W., Boulton J.S., Hurle D.T.J. 1962. *Solid-State Electronics*, **5**: 395.

41. Flemings M.C. 1974. *Solidification Processing*, pp. 58-92. New York: McGraw-Hill Book Company. 364 pp.

42. Tiller W.A., Jackson K.A., Rutter J.W., Chalmers B. 1953. *Acta Metallurgica*, **1**: 428-437.

43. Kasper E. 1996. *Applied Surface Science*, **102**: 189.

44. Ellis S.G. 1955. *Journal of Applied Physics*, **26**: 1140.

45. Lan C.W., Liang M.C. 1998. *Journal of Crystal Growth*, **186**: 203.

46. Xing Z.J., Kennedy J.K., Witt A.F. 1984. *Journal of Crystal Growth*, **68**: 776.

47. Bliss D., Demczyk B., Anselmo A., Bailey J. 1997. *Journal of Crystal Growth*, **174**: 187.